

Design Space Exploration of Microring Resonators in Silicon Photonic Interconnects: Impact of the Ring Curvature

Meisam Bahadori, *Student Member, IEEE*, Mahdi Nikdast, *Member, IEEE*, Sébastien Rumley, Liang Yuan Dai, Natalie Janosik, Thomas Van Vaerenbergh, Alexander Gazman, Qixiang Cheng, Robert Polster, and Keren Bergman, *Fellow, IEEE, Fellow, OSA*

Abstract—A detailed analysis of fundamental trade-offs between ring radius and coupling gap size is presented to draw realistic borders of the possible design space for microring resonators (MRRs). The coupling coefficient for the ring-waveguide structure is estimated based on an integration of the non-uniform gap between the ring and the waveguide. Combined with the supermode analysis of two coupled waveguides, this approach is further expanded into a closed-form equation that describes the coupling strength. This equation permits to evaluate how the distance separating a waveguide from a ring resonator, and the ring radius, affect coupling. The effect of ring radius on the bending loss of the ring is furthermore modeled based on the measurements for silicon MRRs with different radii. These compact models for coupling and loss are subsequently used to derive the main optical properties of MRRs such as 3dB optical bandwidth, extinction ratio of resonance, and insertion loss, hence identifying the design space. Our results indicate that the design space for add-drop filters in a wavelength division multiplexed link is currently limited to 5 to 10 μm in radius and gap sizes ranging from 120 nm to 210 nm. The good agreement between the results from the proposed compact model for coupling and the numerical FDTD and experimental measurements indicate the application of our approach in realizing fast and efficient design space exploration of MRRs in silicon photonic interconnects.

Index Terms—Silicon photonics, microring resonators, design space exploration, coupling strength, finite difference time domain, compact models, waveguides, discretization, design space, optical loss, wavelength, bending loss, optical power budget

I. INTRODUCTION

MICRORING resonators (MRRs) are often presented as the workhorse of future architectures for integrated optical interconnects based on high-speed silicon photonics [1], [2]. The compact footprint of a microring (e.g. radius $\sim 5 \mu\text{m}$), and its capability of performing variety of functions, such as filtering [3]–[5], modulation [6], [7], wavelength-selective dropping [5], [8], and spatial switching [9], [10] are all merits of such silicon-based structures. It is therefore no wonder that the path to commercialization of silicon photonics has had a major overlap with the development of passive and active microring-based structures [11]–[13] suitable for

wavelength division multiplexed (WDM) applications. Despite their susceptibility to temperature variations due to the large thermo-optic coefficient of silicon [14], [15], MRRs equipped with integrated microheaters [16], [17] and feedback control loops [18], [19] have shown resilient behavior to ambient thermal fluctuations or thermal crosstalk among co-located devices. The same thermal principle has shown advantages in performing low-speed modulation [20] and switching on a micro-second time scale [21], [22]. Using a diode type junction (i.e. PIN or PN) for carrier injection or depletion, nanosecond-scale tunability and switching have also been realized with MRRs [23], [24].

These appealing features have led to a variety of recent proposed WDM transmitters and receivers based on MRRs [25]–[27]. Numerous MRR-based network architectures, acting as Photonic Networks-on-Chip (PNoCs), have also been promoted [28], [29]. In these designs, the MRR frequently appears as a discrete component achieving a specific function (e.g. selection of a single wavelength) at the cost of a predetermined power penalty [30], [31]. For an architecture to remain feasible, the sum of all such power penalties must remain in a certain range such that the link power budget is not exceeded. The sum of inflicted power penalties also has an impact on the architecture power efficiency [32]. The incentive is thus strong to minimize power penalties of each individual MRR, no matter if used for modulation [33], demultiplexing [33], [34], or switching [35].

Optimization of microrings' power penalty, however, demands a deeper understanding of how these structures operate. Hence, MRRs are subject to multiple constraints. On one hand, the radius must be large enough to prevent undesired high bending losses (i.e. radiation and scattering), especially when used in a drop configuration, but must also remain small enough to avoid multiple resonances in the optical bandwidth of interest [36]. On the other hand, their coupling to the adjacent waveguides must be strong enough to capture the signal of interest. More specifically and for instance, the 3dB bandwidth of a ring used in a WDM add-drop configuration should be large enough to accommodate the bandwidth of the optical signal to be dropped. A too narrow bandwidth will result in heavy, and undesired, truncation of the signal spectrum, thus distortions [33] (truncation power penalty). However, the same 3dB bandwidth should not be too large to avoid capturing parts of other signals in addition to the one to drop. A too large bandwidth can cause a severe crosstalk

M. Bahadori, S. Rumley, L. Y. Dai, N. Janosik, A. Gazman, Q. Cheng, R. Polster, and K. Bergman are with the Department of Electrical Engineering, Columbia University, New York, NY 10027, USA. Email: mb3875@columbia.edu

M. Nikdast is with the Department of Electrical and Computer Engineering, Colorado State University, Fort Collins, CO, USA.

T. Van Vaerenbergh is with Hewlett Packard Labs, Hewlett Packard Enterprise, 3000 Hanover St, CA94304 Palo Alto, CA, USA.

problem (crosstalk power penalty) if the channel density is high [34], [37]–[39].

Under these multiple constraints, the selection of a ring with right parameters, although a must, is not a straightforward process. For example, a larger radius results in a strong coupling of the ring to the waveguides (increasing 3dB bandwidth) while at the same time it results in a smaller optical loss of the ring (decreasing 3dB bandwidth) [38]. Furthermore, in some cases no realistic MRR matching all the requirements exists. Methods enabling photonic architecture designers to identify whether rings matching different requirements can be fabricated, and how they should be designed, are therefore highly required.

In this paper, we propose such a method, and introduce two compact models underlying this method. The first model, detailed in Section III, aims at predicting how the optical mode coupling effect present at the interface between a ring and a waveguide is affected by geometrical parameters, namely the ring-waveguide distance (i.e. minimum gap size between the ring and the waveguide) and ring radius. The second model (Section IV) relates the optical loss observable in the ring to its diameter. We then exemplify how our method can ease the selection of ring design parameters in Section V. But prior to presenting the specifics of each model, we briefly review former work on ring resonator modeling in the next Section.

II. RING RESONATOR MODELING

The most accurate and complete way to explore the design space of ring resonators (i.e. estimation of the coupling strength and radiation loss) is by means of brute-force full-wave methods, such as three-dimensional finite-difference-time-domain (3D FDTD) [40]–[42] or finite-element method (FEM) [43], [44]. As shown in Fig. 1, such numerical simulations do not include any intermediate steps and once setup, they can directly calculate the desired parameters. Although attractive for simulating structures of limited complexity, these methods are based on time-consuming calculation procedures, which render them rather ineffective when applied to complex structures such as higher-order MRR filters [8], [45]. Even for a simple MRR structure, the coupling strength between the ring and the bus waveguides depends on multiple parameters, namely the width and height of waveguides, radius of the ring, the wavelength of operation, and the gap between the ring and the waveguide. This complexity makes the design space exploration of MRRs by means of FDTD or FEM simulations particularly cumbersome.

Alternatively, the design space of MRRs can be explored by means of abstract compact models. A ring of the radius R can be defined by a loss coefficient α in units of cm^{-1} or dB/cm (hence a round-trip loss of $L = \exp(-2\pi R \alpha_{1/\text{cm}})$ or $L_{\text{dB}} = 2\pi R \alpha_{\text{dB/cm}}$), and one (all-pass configuration), two (first-order add-drop configuration), or even more (higher-order add-drop configuration [8]) through and cross coupling coefficient(s) (t and κ – unitless parameters) describing the coupling strength of the electric and magnetic fields inside the ring with the adjacent waveguide(s). As long as the coupling between the ring and waveguides is assumed lossless, the

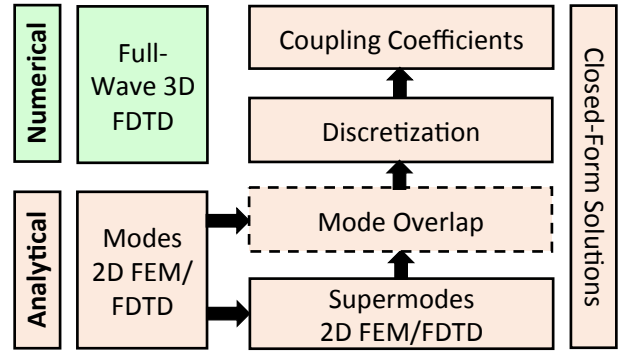


Fig. 1. Comparison between the numerical method and our proposed analytical method for estimating the coupling between a ring and a waveguide. A fully numerical approach requires only one step while our analytical approach requires intermediate steps for calculating optical modes. In return, the analytical approach provides closed-form solutions for the coupling coefficients.

relation $\kappa^2 + t^2 = 1$ holds, hence knowing only one of the two parameters is sufficient. These models are key to understand the dynamics of the resonant behavior [46], and to quickly seize the principles at play for a large-scale system. However, they do not capture the relationships between the physical dimensions of the structure, the fabrication-induced effects, and the coefficients used. As further discussed by Nikdast *et al.* [47], Le Maitre *et al.* [48], and Lu *et al.* [49] fabrication-induced effects are of major importance when a structure as compact as a MRR is considered. Compact models agnostic to the physical dimensions of the structure are thus insufficient to clearly assess the capabilities of MRRs for silicon photonic interconnects in practice. This motivates us to establish accurate yet efficient models to bridge the gap between abstract compact models, time-consuming full-wave simulations, and the fabrication aspects of MRRs for silicon-on-insulator (SOI) platform. The resulting models allow us to sweep a design space corresponding to different wavelengths, ring radii, and coupling gap sizes. For each considered ring, we calculate various figures of merit and exclude the designs failing to fulfill a set of minimal requirements. Finally, by considering the remaining “realm of feasibility”, we derive conclusions on MRR capabilities. To the best of our knowledge, this is the first time that such comprehensive design space exploration of ring resonators in SOI platform is presented in the literature.

As shown in Fig. 1, our proposed approach for estimating coupling coefficients requires some intermediate steps for calculating the optical modes of the waveguides [see Fig. 1]. This can be realized by building a waveguide cross-section specific database of effective indices inside an isolated waveguide (for different wavelengths), as well as inside a coupled pair of waveguides (for different wavelengths and gaps) as described below:

A. Database for optical modes of isolated waveguides

We used COMSOL [50] software to numerically calculate the effective index n_{eff} of the fundamental mode (quasi-TE₀₀) of a straight silicon waveguide by sweeping the wavelength from 1500 nm to 1600 nm (on 2.5 nm steps) and then linearly interpolated. Subsequently, the group index of the waveguide

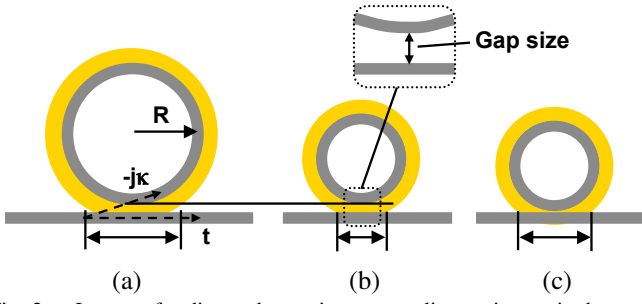


Fig. 2. Impact of radius and gap size on coupling region. κ is the cross coupling coefficient and t is the through coupling coefficient. (a) and (b) have the same gap sizes but the larger radius of (a) results in a larger interaction region. Therefore, the cross coupling coefficients in (a) and (b) are not the same. (b) and (c) have the same radius, but the smaller gap size in (c) results in a larger interaction region.

is also calculated from the equation $n_g = n_{\text{eff}} - \lambda dn_{\text{eff}}/d\lambda$. The dispersion of silicon and silica is taken into account with Sellmier equation:

$$n^2 - 1 = \frac{A_1 \lambda^2}{\lambda^2 - B_1^2} + \frac{A_2 \lambda^2}{\lambda^2 - B_2^2} + \frac{A_3 \lambda^2}{\lambda^2 - B_3^2} \quad (1)$$

The coefficients for silicon are set to $A_1 = 10.6684$, $A_2 = 0.003$, $A_3 = 1.5413$, $B_1 = 0.3015$, $B_2 = 1.1347$, $B_3 = 1104$, and the coefficients for silica are set to $A_1 = 0.6961$, $A_2 = 0.4079$, $A_3 = 0.8974$, $B_1 = 0.0684$, $B_2 = 0.1162$, $B_3 = 9.8961$ (note that λ is in μm units) [51].

B. Database for optical modes of waveguide pairs

We used COMSOL [50] to create a database of the effective indices of the even and odd supermodes in order to deliver an even and odd index for any gap and wavelength using interpolation. To populate this database, the coupling gap distance separating the coupled straight waveguides is swept from 50 nm to 1000 nm (on a step of 5 nm) while the wavelength is swept from 1500 nm to 1600 nm on the step of 2.5 nm.

III. MODELING OF RING-WAVEGUIDE COUPLING

In this section, a compact modeling methodology is presented for the fundamental parameters of the MRR structures: the ring cross coupling coefficient, κ , and through coupling coefficient, t . We start by discretizing the nonuniform coupling region between the ring resonator and the waveguide into many short regions, and treating each small region as a uniform directional coupler whose cross and through coupling coefficients are well known [51], [52]. By accumulating the coupling effects of all the small coupling elements, an estimation of the coupling strength of MRRs can be obtained through a Riemann sum leading to a continuous integral form. As we will see, the accuracy of the proposed approach is confirmed both by FDTD simulations and our fabricated MRR structures through AIM Photonics [53].

In all that follows, it is assumed that the ring and the adjacent coupling waveguides have identical cross-sections (i.e. same width and height). As further explained in Appendix I, this will remove the need to calculate mode overlap integrals in our intermediate steps [see also Fig. 1] and will result in compact closed-form equations for the coupling coefficients.

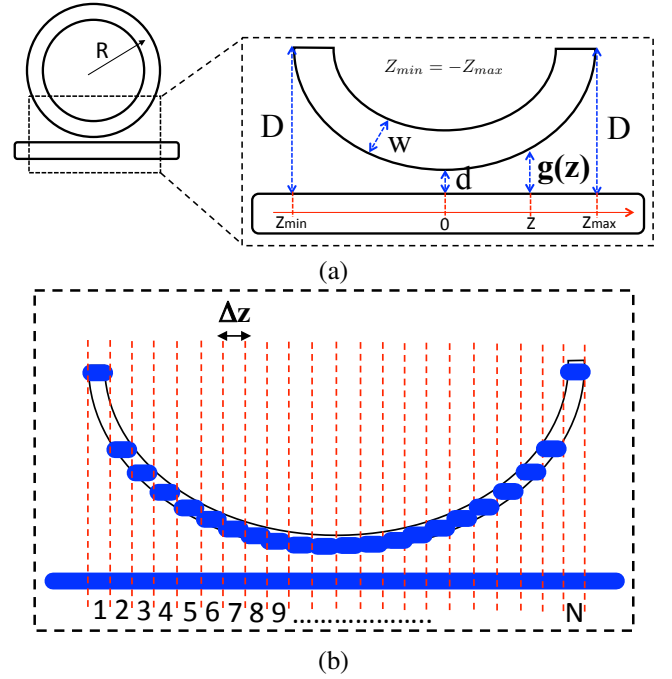


Fig. 3. (a) Schematic of non-uniform coupling between the ring and the waveguide. It is assumed that $D = 1000$ nm and there is no coupling between the ring and the bus waveguide beyond D . (b) Discretization of the non-uniform coupling region between the ring and the waveguide. By letting $N \rightarrow \infty$ over the finite coupling region, the discretization leads to an integral form.

A. Estimation of Coupling Coefficient

Considering a rectangular cross-section for the silicon waveguides (e.g. 450×220 nm Si surrounded by SiO_2 cladding), we intend to capture the dependence of the cross and through coupling coefficients (κ and t) on the ring radius and the gap size (minimum distance between the ring and the waveguide as shown in Fig. 2). Although it is obvious that κ has a strong dependence on the gap [40], which is typically described by an exponential fitting [54], [55], its dependence on the radius is not clear at first glance. Fig. 2 demonstrates the impact of radius and the coupling gap size on the ring-waveguide electric field coupling coefficients. The colored area around each ring indicates the decaying tail of the optical mode inside the ring. Although this tail is infinite in practice, for the sake of the example, let us assume that no coupling occurs beyond the colored region. Fig. 2(a) and Fig. 2(b) have the same gap size, but the larger radius of the ring in Fig. 2(a) results in a larger coupling interaction region between ring and waveguide (denoted by double-arrow). A larger interaction region then leads to a larger cross coupling coefficient (κ) since the coupling at the closest proximity between the ring and the waveguide is more uniform. Fig. 2(b) and Fig. 2(c) have the same radius, but the smaller gap in Fig. 2(c) results in a larger coupling region, hence a stronger coupling.

As shown in Fig. 3(a), the coupling gap along the coupling region, $g(z)$, can be estimated by the following equation:

$$g(z) = d + (R + w/2) - \sqrt{(R + w/2)^2 - z^2} \quad (2)$$

where R is the radius of the ring (center to midpoint), w is the width of the ring, d is the minimum gap distance between the ring and the waveguide, and z is the distance relative to

the point where the gap distance is at its minimum. Note that $g(0) = d$, and $g(R + w/2) = d + (R + w/2)$. Assuming that the coupling is only significant within a distance D ($\approx 1 \mu\text{m}$) [see Fig. 3(a)], the length of the coupling region is thus $Z_{\max} - Z_{\min} = 2 Z_{\max}$ as $Z_{\min} = -Z_{\max}$ due to the symmetry, with

$$Z_{\max} = \sqrt{(D - d)(2(R + w/2) - (D - d))}. \quad (3)$$

It is clear that unlike a directional coupler made of two straight waveguides where the coupling region is uniform, due to the curvature of the ring structure, the coupling region formed between the ring and the waveguide is nonuniform. To properly capture the through and cross coupling coefficients of the structure (t and κ), this non-uniformity must be taken into account.

To this aim, consider a uniform discretization of the non-uniform region into N very small intervals of size $\Delta z = (Z_{\max} - Z_{\min})/N$ in the z direction, as shown in Fig. 3(b). The gap distance corresponding to each position on the z -axis (i.e. z_i , $i = 1, 2, \dots, N$), denoted by g_i , can be obtained from Eq. (2). Assuming the i^{th} interval extends from z_{i-1} to z_i , its corresponding gap can be estimated by $g_i = g((z_{i-1} + z_i)/2)$. Small intervals permit to consider a uniform coupling within each interval. We then write the transfer matrix of the i^{th} interval [see Appendix I] as

$$T_i = \exp(-j\phi_i) \begin{bmatrix} t_i & -j\kappa_i \\ -j\kappa_i & t_i \end{bmatrix} \quad (4)$$

where

$$\phi_i = \frac{2\pi}{\lambda} \Delta z \frac{n_{\text{even}}[g_i] + n_{\text{odd}}[g_i]}{2}, \quad (5a)$$

$$t_i = \cos\left(\frac{2\pi}{\lambda} \Delta z \frac{n_{\text{even}}[g_i] - n_{\text{odd}}[g_i]}{2}\right), \quad (5b)$$

$$\kappa_i = \sin\left(\frac{2\pi}{\lambda} \Delta z \frac{n_{\text{even}}[g_i] - n_{\text{odd}}[g_i]}{2}\right). \quad (5c)$$

In these equations, $n_{\text{even}}[g_i]$ and $n_{\text{odd}}[g_i]$ are the effective indices of the even and odd supermodes as a function of the gap distance g_i at a given wavelength. For an identical pair of coupled waveguides, these functions can be fitted by exponential curves as a function of gap size, and thus be written as

$$n_E \approx n_{\text{eff}} + a_E \exp(-\gamma_E g) \quad (6)$$

for the even mode, and

$$n_O \approx n_{\text{eff}} - a_O \exp(-\gamma_O g) \quad (7)$$

for the odd mode [see Appendix II]. n_{eff} is the effective index of the optical mode of each waveguide in the absence of coupling.

The full impact of the coupling region can then be evaluated by cascading the intervals, thus by multiplying the transfer matrices of all the intervals. The resulting global transfer matrix $T = T_N \times T_{N-1} \times \dots \times T_2 \times T_1$, has the same form as Eq. (4) due to the identity

$$\begin{bmatrix} \cos(A) & -j\sin(A) \\ -j\sin(A) & \cos(A) \end{bmatrix} \times \begin{bmatrix} \cos(B) & -j\sin(B) \\ -j\sin(B) & \cos(B) \end{bmatrix} = \begin{bmatrix} \cos(A+B) & -j\sin(A+B) \\ -j\sin(A+B) & \cos(A+B) \end{bmatrix} \quad (8)$$

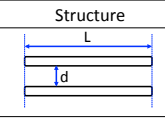
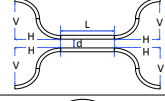
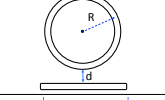
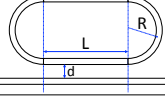
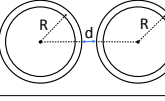
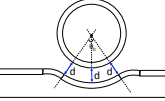
| Structure | x | $B(x)$ |
|--|--|---|
|  | γL | x |
|  | γL | $x \left[1 + \frac{2H}{L} \exp\left(-\frac{V}{L}x\right) I_0\left(\frac{V}{L}x\right) \right]$ |
|  | $\gamma\left(R + \frac{w}{2}\right)$ | $\pi x \exp(-x) [I_1(x) + L_{-1}(x)]$ $\approx \sqrt{2\pi x}$ |
|  | $\gamma\left(R + \frac{w}{2}\right)$ | $\frac{L}{R + \frac{w}{2}} x + B_{\text{ring-wg}}(x)$ |
|  | $\gamma\left(R + \frac{w}{2}\right)$ | $0.5 B_{\text{ring-wg}}(2x)$ |
|  | $\gamma\left(R + \frac{w}{2} + \frac{d}{2}\right)\theta$ | x |

Fig. 4. Summary of the curvature function of the coupling for different structures including uniform and circular coupling regions. The coupling coefficient is then found from Eq. (11) and Table 1.

and is given by

$$T = \exp(-j\phi_+) \begin{bmatrix} \cos(\phi_-) & -j\sin(\phi_-) \\ -j\sin(\phi_-) & \cos(\phi_-) \end{bmatrix} \quad (9)$$

where

$$\phi_+ = \frac{2\pi}{\lambda} \sum_{i=1}^N \frac{n_{\text{even}}[g_i] + n_{\text{odd}}[g_i]}{2} \Delta z, \quad (10a)$$

$$\phi_- = \frac{2\pi}{\lambda} \sum_{i=1}^N \frac{n_{\text{even}}[g_i] - n_{\text{odd}}[g_i]}{2} \Delta z. \quad (10b)$$

Therefore coupling coefficients (t and κ) are obtained simply by inspecting the elements of T matrix in Eq. (9), i.e. $t = \cos(\phi_-)$ and $\kappa = \sin(\phi_-)$. In the limit where $N \rightarrow \infty$, the summation in these equations turns into an integral since $\Delta z \rightarrow 0$. As shown in Appendix II, the result of the integration for kappa is given by

$$\kappa = \sin\left(\frac{\pi}{\lambda} \left[\frac{a_E}{\gamma_E} e^{-\gamma_E d} B(x_E) + \frac{a_O}{\gamma_O} e^{-\gamma_O d} B(x_O) \right]\right) \quad (11)$$

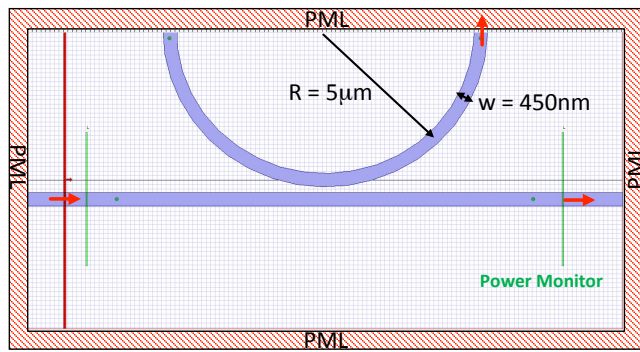
where a_E , a_O , γ_E , γ_O are the parameters of the fitted exponential curves of Eq. (6) and (7), which are independent of the shape of the coupling region. We define $B(x)$ as the curvature function of the coupling region and is given by

$$B(x) = 2x \int_0^{\pi/2} \exp(-x(1 - \cos\theta)) \cos\theta d\theta \quad (12)$$

for the ring-waveguide structure in Fig. 3. Eq. (12) has a closed-form solution given by

$$B(x) = \pi x \exp(-x) [I_1(x) + L_{-1}(x)] \quad (13)$$

in which $I_1(x)$ is the modified Bessel function of the first kind of order 1 and $L_{-1}(x)$ is the modified Struve function of the



(a)

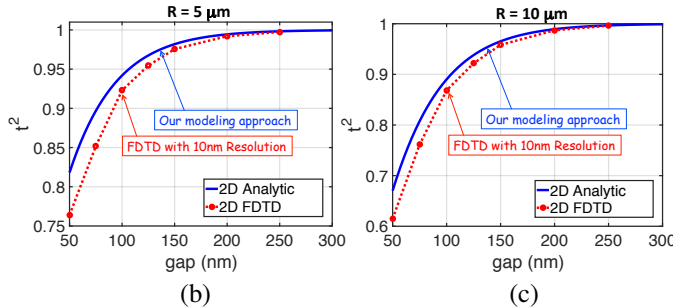


Fig. 5. (a) Schematic of the 2D FDTD with perfectly matched layers (PML) boundary conditions for the coupling of waveguide to the ring resonator. (b) Thru transmission as a function of gap for 5 μm radius at 1550 nm wavelength. (c) Thru transmission as a function of gap for 10 μm at 1550 nm wavelength.

first kind of order -1. Based on the asymptotic behavior of $I_1(x)$ and $L_{-1}(x)$ functions for large x , it can be verified that

$$B(x) \approx \sqrt{2\pi x}. \quad (14)$$

The parameters of function $B(x)$ in Eq. (11), and therefore in Eq. (13) are given by $x_E = \gamma_E(R + w/2)$ and $x_O = \gamma_O(R + w/2)$. Noting finally that since in general the argument of $\sin(\dots)$ function in Eq. (11) is small for coupling of ring to the waveguide, the approximation $\sin(t) \approx t$ can be applied:

$$\kappa \approx \frac{\pi}{\lambda} \left[\frac{a_E}{\gamma_E} e^{-\gamma_E d} B(x_E) + \frac{a_O}{\gamma_O} e^{-\gamma_O d} B(x_O) \right]. \quad (15)$$

Equation (11) is sufficient to fulfill our initial goal of evaluating κ as a function of radius and gap. It is worth noting that radius only appears in the $B(x)$ function in Eq. (11). In fact, the effect of the non-uniform coupling is solely captured by $B(x)$, and the four parameters a_E , a_O , γ_E , γ_O do not depend on the shape of the coupling region. For example, if a uniform coupling of length L and gap d between two straight waveguides is considered, $B(x) = x$ is obtained where $x_{E,O} = \gamma_{E,O}L$. Appendix III provides details of calculating $B(x)$ for other structures such as race-track rings, and ring-ring coupling in higher order add-drop filters. The results are summarized in Fig. 4.

B. Model vs. FDTD for 2D Structures

We now aim at validating Eq. (11) against finite-difference time-domain (FDTD) simulations. We set up a 2D FDTD simulation of 450 nm wide slab waveguides with 10 nm grid resolution in OptiFDTD software from OptiWave [56], in order to numerically evaluate the coupling coefficients (t and κ) of the ring-waveguide structure. Fig. 5(a) shows the

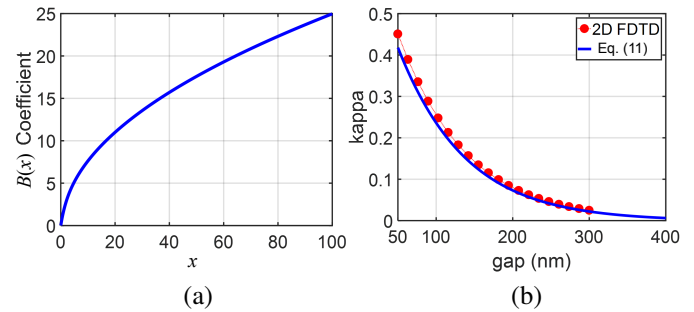


Fig. 6. (a) Numerical evaluation of the circular curvature function $B(x)$ given in Eq. (11). (b) Comparison of results from model and 2D FDTD for $R = 5 \mu\text{m}$, $w = 450 \text{ nm}$ and various coupling gaps.

simulated structure consisting of a straight waveguide and half of a ring resonator. Perfectly matched layers (PML) boundary conditions are applied for the unidirectional transmission. Power monitors are placed at the input and output ports of the bus waveguide. Fig. 5(b) shows the comparison between our approach and FDTD as a function of gap size for 5 μm radius at 1550 nm wavelength. A maximum error of 5% is observed for 50 nm gap size while the error is progressively decreasing as the gap size is increased. This further advocates the validity of our model since fabricating gap sizes less than 100 nm is typically difficult and avoided. Fig. 5(c) shows the same plot for 10 μm radius. A larger radius results in a smaller through transmission, hence stronger cross coupling of power from the waveguide into the ring resonator. It is seen that Eq. (11) provides more accurate results for a larger radius.

For the 2D example of 5 μm radius at 1550 nm wavelength, the coefficients of the model in Eq. (11) are extracted by a nonlinear least mean square error curve fitting as $a_E = 0.141188$, $a_O = 0.092605$, $\gamma_E = 0.012756 \text{ nm}^{-1}$, $\gamma_O = 0.010761 \text{ nm}^{-1}$, therefore $x_E = 66.65$, and $x_O = 56.2254$. Fig. 6(a) shows a plot of the curvature function $B(x)$ as a function of x . Fig. 6(b) plots Eq. (11) against the results of 2D FDTD with 5 nm mesh size for $R = 5 \mu\text{m}$ based on the extracted parameters of the modes and the curvature function. A very good agreement is observed.

C. Model vs. FDTD for 3D Structures

Next, we examine our analytical approach for a 3D case where the rings and waveguides are all made of silicon strip waveguides with $450 \times 220 \text{ nm}$ cross-section. The modes of a single waveguide and the supermodes of two coupled waveguides are calculated from COMSOL software as shown in Fig. 7(a) for two identical waveguides. For this example, the parameters of the model are extracted as $a_E = 0.177967$, $a_O = 0.049910$, $\gamma_E = 0.011898 \text{ nm}^{-1}$, $\gamma_O = 0.006601 \text{ nm}^{-1}$, $x_E = 62.1671$, $x_O = 34.49$ for $R = 5 \mu\text{m}$ at $\lambda = 1550 \text{ nm}$, and then the curvature coefficients are calculated as $B(x_E) = 19.64$, and $B(x_O) = 14.57$. Table 1 summarizes the parameters of the model for $400 \times 220 \text{ nm}$, $450 \times 220 \text{ nm}$, and $500 \times 220 \text{ nm}$ strip waveguides at $\lambda = 1550 \text{ nm}$. It is seen that a_E and a_O have a stronger dependence on the width of the waveguide than γ_E and γ_O . Fig. 7(b) shows the result of estimating t and κ with Eq. (11) at 1550 nm wavelength for 5 μm, 10 μm, and 20 μm radii. As can be observed, the curvature of the coupling region (i.e. the radius of the ring) has

TABLE I

PARAMETERS OF THE COUPLING MODEL FOR THE FUNDAMENTAL QUASI-TE₀₀ MODE OF SILICON STRIP WAVEGUIDES AT $\lambda = 1550$ NM.

| WG Size | 400×220 | 450×220 | 500×220 |
|------------|----------|----------|----------|
| a_E | 0.242422 | 0.177967 | 0.132273 |
| a_O | 0.077526 | 0.049910 | 0.033840 |
| γ_E | 0.010687 | 0.011898 | 0.012783 |
| γ_O | 0.006129 | 0.006601 | 0.006911 |

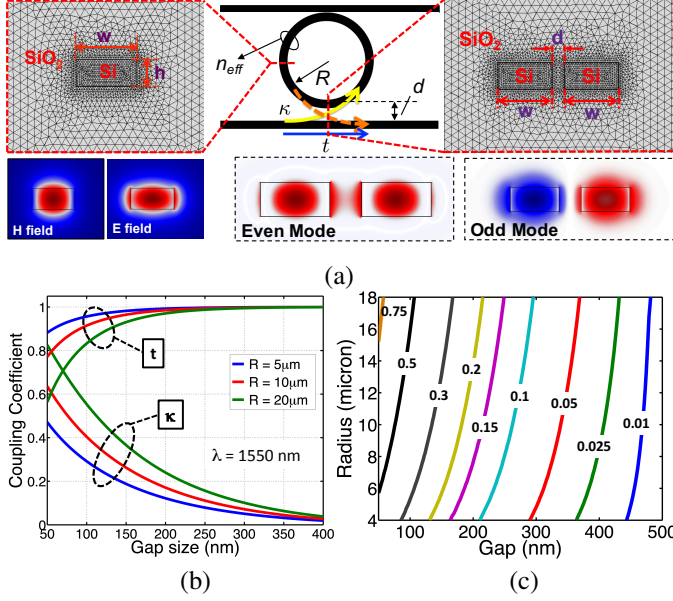


Fig. 7. (a) Schematic of a ring resonator with two coupling waveguides. The cross-section of single strip and coupled strip waveguides and the mode profiles from COMSOL are also shown. The strip waveguides are 450×220 nm. (b) Coupling coefficients (κ and t) as a function of coupling gap at 1550 nm with three different radii. (c) Contours of κ for various gap sizes and radii at 1550 nm.

a noticeable effect on the coupling coefficients. Fig. 7(c) plots the contours of kappa (cross coupling) as a function of gap and radius of the ring. Even though they approach a vertical line for very large radii, these contours are clearly non-vertical for smaller radii, demonstrating the significant effect of the radius on the coupling strength in that regime.

Next, we performed a series of 3D FDTD simulations with 10 nm grid size with Lumerical FDTD software [57]. To show the effect of three main physical parameters of the structure, i.e. gap, radius, and width of the waveguide, the wavelength of operation was set to the fixed value of 1550 nm. The structure in the simulations is the 3D version of the one shown in Fig. 5(a). First, the cross-section of the waveguide was set to 400×220 nm and then the FDTD simulations were performed by sweeping the gap size from 50 nm to 400 nm on the step size of 50 nm for various radii. Fig. 8(a) and Fig. 8(b) show the dependence of κ and t as a function of gap size for $R = 5 \mu\text{m}$ and $R = 10 \mu\text{m}$, respectively. A good agreement is observed between our analytical model and 3D FDTD results. As expected, a larger radius results in a stronger coupling between the ring and waveguide, hence a larger value for κ . Next, the cross-section of the waveguide was set to 450×220 nm and the simulations were performed again. Fig. 8(c) and Fig. 8(d) depict the results for $R = 5 \mu\text{m}$ and $R = 10 \mu\text{m}$,

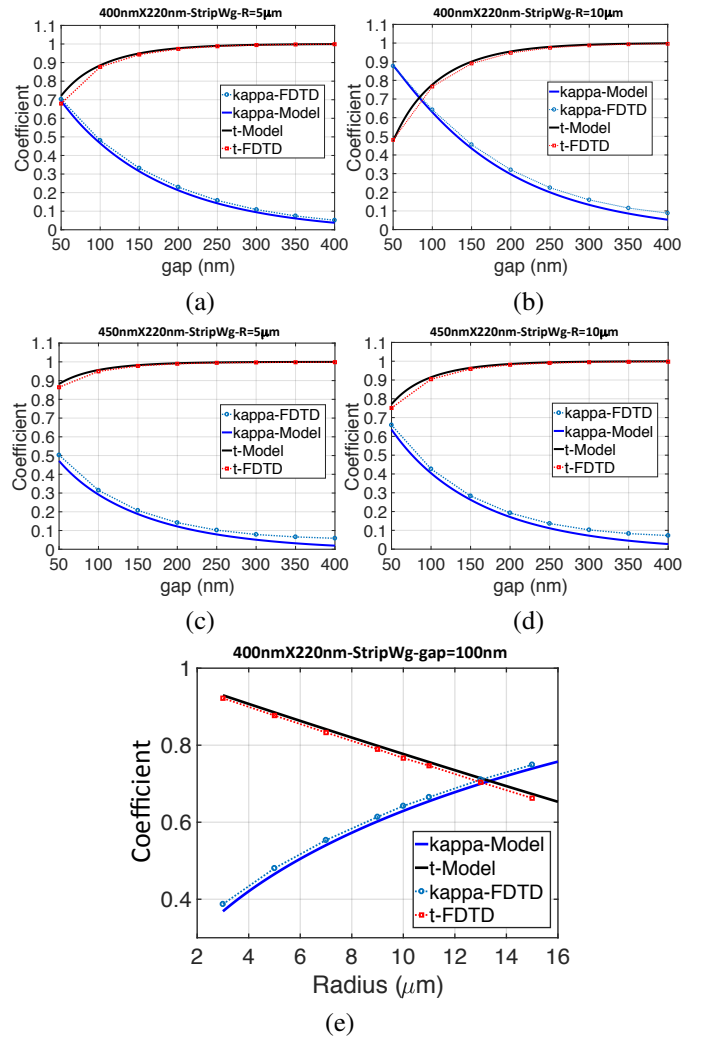


Fig. 8. (a) Comparison of predicted ring-waveguide coupling coefficients (solid lines) and the 3D FDTD simulations (circled dotted) for $R = 5 \mu\text{m}$ and $w = 400$ nm. (b) $R = 10 \mu\text{m}$ and $w = 400$ nm. (c) $R = 5 \mu\text{m}$ and $w = 450$ nm. (d) $R = 10 \mu\text{m}$ and $w = 450$ nm. (e) Dependence of coupling coefficients on the radius of the ring for gap = 100 nm and $w = 400$ nm. The proposed model accurately captures the effect of radius as it closely resembles the results of full-wave 3D FDTD simulations.

respectively. Compared to Fig. 8(a) and Fig. 8(b) it is seen that both the model and FDTD predict a weaker coupling as the width of the waveguide increases. This is due to the fact that the fundamental optical mode inside a wider waveguide has a higher effective index, hence it is more confined within the silicon core and its exponential tail outside the core is shorter. Finally, to demonstrate the effect of radius on the coupling strength, we set the gap size to 100 nm and swept the radius from 3 μm to 15 μm . The results are shown in Fig. 8(e) for both FDTD and our model. A very good agreement is observed indicating that our proposed model in Eq. (11) fully captures the effect of physical parameters on the coupling strength. Since radius only appears in the curvature function $B(x)$ in Eq. (11), the concluded rule-of-thumb is that ring-waveguide coupling coefficient scales up as the *square-root of the radius*. For example, increasing the radius by a factor of two (e.g. going from 5 μm to 10 μm) while maintaining the same gap size and waveguide dimensions will increase the kappa by a

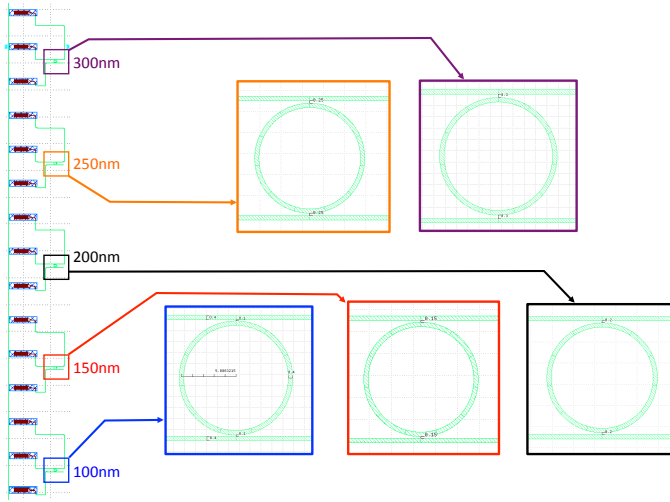


Fig. 9. Layout of fabricated silicon rings through AIM Photonics MPW run (2016). This figure shows symmetric add-drop structures with $5 \mu\text{m}$ radius and gap sizes varying from 100 nm to 300 nm in 50 nm steps. The layout also shows the TE-polarized vertical grating couplers used for coupling light in and out. Each add-drop ring is connected to three grating couplers in this design.

factor of $\sqrt{2}$. This can be easily verified in Fig. 8(e).

D. Model vs. Experimental Results

After validating our model of ring-waveguide coupling against full-wave FDTD simulations, three batches of test structures based on add-drop configurations were designed and fabricated through AIM Photonics [53] multi-project wafer run. The waveguides were chosen to be 400×220 nm strip waveguides since a 400 nm width will provide the strongest coupling coefficients. We used the “gdspsy” open source library [58] to create the layout of the test structures. The first batch of structures have radii of $5 \mu\text{m}$ while the second and third batches are designed with $7.5 \mu\text{m}$ and $10 \mu\text{m}$ radii. Each batch includes five symmetric add-drop structures (i.e. input gap size = drop gap size) set to 100 nm, 150 nm, 200 nm, 250 nm, and 300 nm. Fig. 9 shows the GDS layout of the first batch with $5 \mu\text{m}$ radius. TE-polarized vertical grating couplers were used to couple the light in and out of the silicon chip. Each add-drop structure is connected to three grating couplers for monitoring both the through spectral response and the drop spectral response.

The through and drop transmissions responses for the add-drop structure are given by [36]

$$TR = \left| \frac{t_{in} - t_{drp} \sqrt{L} \exp(-j\delta\phi)}{1 - t_{in} t_{drp} \sqrt{L} \exp(-j\delta\phi)} \right|^2 \quad (16a)$$

$$DR = \left| \frac{\kappa_{in} \kappa_{drp} L^{0.25} \exp(-j\delta\phi/2)}{1 - t_{in} t_{drp} \sqrt{L} \exp(-j\delta\phi)} \right|^2 \quad (16b)$$

where L is the round-trip optical power attenuation inside the ring, t_{in} and t_{drp} are the through coefficient of the input coupling region and the drop coupling region ($t_{in,drp}^2 = 1 - \kappa_{in,drp}^2$), and $\delta\phi$ is the relative phase shift with respect to the

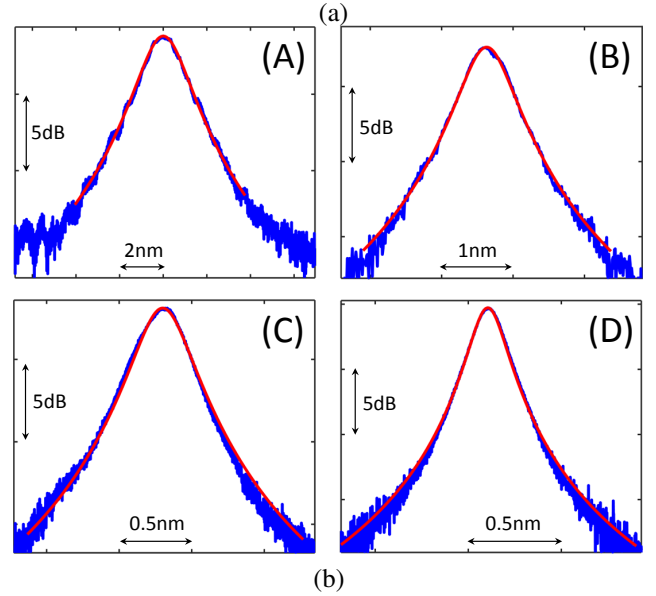
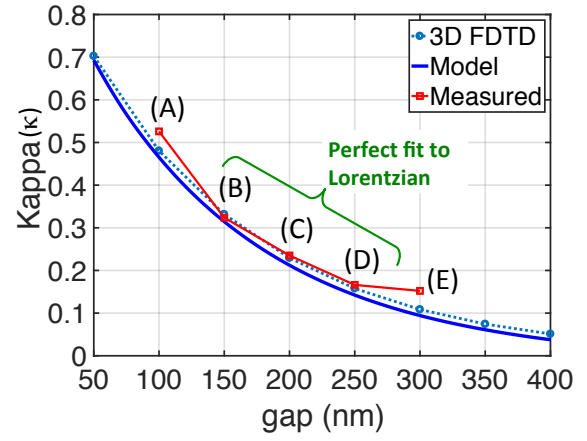


Fig. 10. (a) Comparison of the predicted coupling coefficient (κ) of the ring-waveguide (solid line), the 3D FDTD simulations (dotted circle), and the extracted values by fitting to the Lorentzian response of the drop port of measured spectra. It can be seen that the model has a good agreement with the measurements. (b) Comparison of the measured spectra and the fitted Lorentzian for cases (A), (B), (C), and (D). The last three cases exhibit very good fit.

target resonance:

$$\delta\phi \approx -\frac{\delta\lambda}{FSR_{nm}} \times 2\pi \quad (17)$$

and $\delta\lambda = \lambda - \lambda_{res}$. FSR is the free-spectral range of the resonance spectrum approximated as [36]:

$$FSR_{nm} \approx \frac{\lambda_{res(nm)}^2}{2\pi R_{nm} n_g} \quad (18)$$

The minimum through power (TR_{min}) and the maximum drop power (DR_{max}) is obtained by setting $\delta\phi = 0$ whereas the maximum through power (TR_{max}) and the minimum drop power (DR_{min}) at FSR/2 distance from the resonance is obtained by setting $\delta\phi = \pi$. Finally, the half-power bandwidth (full width at half maximum) of the drop spectrum is given by

$$\Delta\lambda_{3dB} \approx FSR_{nm} \times \frac{1}{\pi} \cos^{-1} \left(1 - \frac{(1 - t_{in} t_{drp} \sqrt{L})^2}{2 t_{in} t_{drp} \sqrt{L}} \right) \quad (19)$$

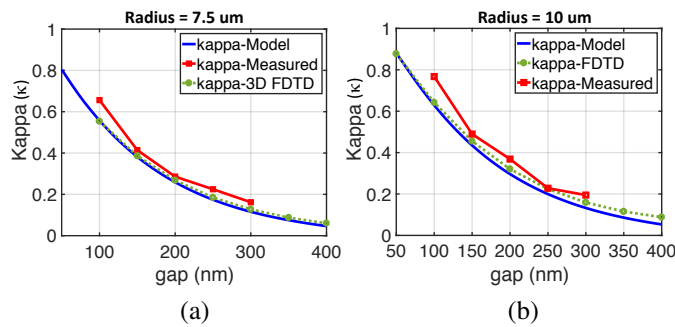


Fig. 11. Comparison of extracted ring-waveguide coupling with the analytical model and FDTD for (a) 7.5 μm radius, and (b) 10 μm radius. As the radius increases, the coupling coefficient increases.

Note that due to the symmetry of all the test structures, it is assumed that $t_{\text{in}} = t_{\text{drp}}$ and $\kappa_{\text{in}} = \kappa_{\text{drp}}$.

In order to extract the coupling of ring-waveguide, we use the drop transmission and perform a least mean square fitting of Eq. (16b) to the measured spectra. Note that in general determining the state of the ring resonator (under-coupled or over-coupled) is not possible without having knowledge of the phase response of the resonator. As pointed out in [59], this leads to an ambiguity in distinguishing between through coupling coefficients and the round-trip loss for all-pass structures (a ring coupled to a single bus waveguide). However, since the test structures were designed to have equal input and drop coupling gaps, the ring resonators will never reach the critical coupling state and should stay under-coupled for any given gap size. The following steps were taken to uniquely extract the coupling coefficients:

- **Step 1:** extract the FSR and 3dB bandwidth of the spectrum by fitting the normalized drop spectrum to the normalized measured spectrum (least-squares fitting).
- **Step 2:** use the extracted bandwidth to find the parameter $\xi = t^2\sqrt{L}$ from Eq. (19).
- **Step 3:** use the measured drop loss at the resonance to establish another relation between t and L .
- **Step 4:** solve the two found equations to uniquely determine t , κ , and L .

Fig. 10(a) shows the extracted ring-waveguide coupling coefficients for 5 μm radius batch. Fig. 10(b) depicts the quality of the spectral fitting to the measured spectra for cases (A), (B), (C), and (D). It is seen that in case (A) the measured spectrum is not smooth around the resonance while in cases (B), (C), and (D) the measured spectra are reasonably smooth. One possible explanation is the strong scattering of light due to the roughness of the sidewalls of the ring in the coupling region between the ring and the waveguide when the gap is 100 nm. The extracted coupling coefficients for these four cases are very close to what our model and 3D FDTD predicts. However, in case (E), corresponding to a gap of 300 nm, the extracted value ($\kappa \approx 0.16$) exhibits a noticeable error when compared to the predicted values ($\kappa \approx 0.1$). The reason for this behavior is the presence of resonance splitting, addressed in the next subsection.

As mentioned in section III-A, the curvature function in Eq. (11) includes the impact of the radius on the coupling coefficients. The predictions of the model in Fig. 7 and Fig.

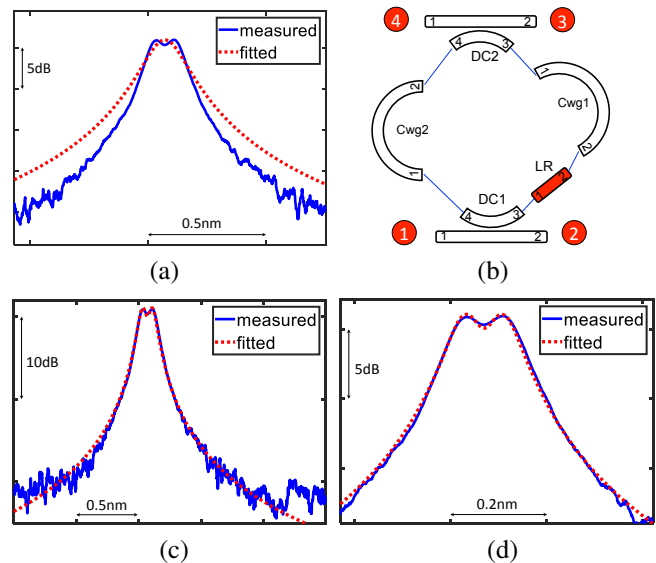


Fig. 12. (a) Comparison of spectral fitting (solid red) to the measured spectrum (solid blue) for $R = 5 \mu\text{m}$ and gap = 300 nm. A clear splitting of resonance is observed. (b) Modeling the backscattering inside the ring by including a lumped reflector. (c) Comparison of the spectral fitting with lumped reflector to the measured spectrum. A very good agreement is observed. (d) Close-up on a small region around the resonance. A symmetric splitting of resonance is observed.

8(e) show that larger radii will result in a stronger cross coupling between the ring and the waveguide. To verify this, the result of the extraction of kappa for $R = 7.5 \mu\text{m}$ and $R = 10 \mu\text{m}$ from our fabricated devices are plotted and compared against the predictions of the model and FDTD in Fig. 11(a) and Fig. 11(b), respectively. For any given coupling gap size, the larger radius clearly provides a stronger coupling coefficient between the ring and the waveguides. Although a more thorough statistical analysis of yield and fabrication variations (e.g. wafer-scale variations) is outside of the scope of this work, but for the given limited dataset we see that the predictions of the model and FDTD closely match the extracted values for kappa.

E. Impact of Back Scattering Inside the Ring

Figure 12(a) depicts the drop spectrum measured in the (E) case (300 nm gap) of Fig. 10(a). As known in the literature [60], the measured spectrum indicates a clear resonance splitting with two peaks when the coupling of the ring to the adjacent waveguide is weak. The red curve on this figure is the fitted spectrum based on Eq. 16(b). Although our fitting procedure appears to be able to decently estimate the 3dB bandwidth of the measured spectrum, it clearly fails to provide a good overall match.

The phenomenon of resonance splitting in microring resonators has been investigated in the literature and its origins have typically been associated with the roughness of the sidewalls of the ring [60]–[63], although recently the presence of the coupling section has been highlighted as a contributor of reflection in rings with smaller gaps [64]. Such roughness causes backscattering of the optical mode that is circulating in one direction inside the ring. The backscattering results in the excitation of a degenerate optical mode circulating in the opposite direction inside the ring. The work presented in

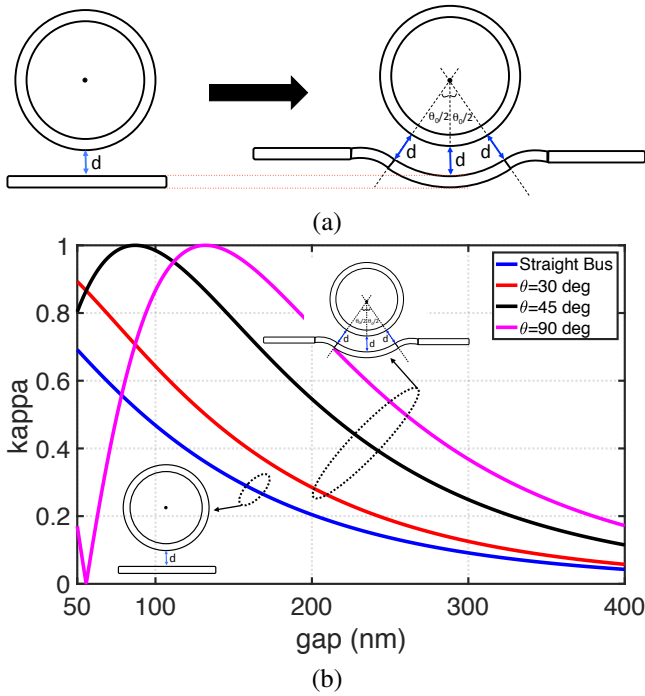


Fig. 13. (a) Transforming the straight bus waveguide into a circular bus. (b) Comparison of ring-waveguide coupling between the case where the bus waveguide is straight and the case where the bus waveguide is circular with the coupling region angle set to 30 degree, 45 degree, and 90 degree. It can be seen that the circular bus provides stronger coupling under similar conditions (same radius and gap size).

[64] has formulated a correction on Eq. 16(b) to include the backscattering effects based on the temporal coupled mode theory, while the work in [60] has proposed an interpretation based on a lumped reflectivity inside the ring. In [64] asymmetric heights of the split resonances were linked to additional reflections in the coupling section. However, in our data the prevalence of symmetric split resonances was observed. Therefore, we choose to model the backscattering effects by a lumped reflector. Fig. 12(b) shows an abstract representation of the structure to which we assimilate the ring. It consists of two lossless directional couplers (DC1 and DC2), two curved waveguides of equal length (Cwg1 and Cwg2) and a lumped reflector (LR) of null length with reflectivity r [see Appendix IV]. The coupling coefficients (t and κ) of the directional couplers and the field reflectivity r of the lumped reflector were then subject to a least mean square fitting to the measured spectrum shown in Fig. 12(a). The result of the curve fitting is shown in Fig. 12(c), which exhibits an almost perfect fit to the measured spectrum. With this correction, the coupling coefficient is now estimated to be $\kappa \approx 0.12$, which is much closer to the predicted value of 0.1. Fig. 12(d) presents a close-up of the fitting result indicating the clear symmetric splitting of the resonance. The backscattering reflectivity was extracted to be $r = 0.0124$. This is well aligned with the conclusion made by Little *et al.* [60] that when $r \geq \kappa^2$, a clear resonance splitting is observed.

F. Coupling region modeling: conclusion

Summarizing this Section, we have presented a mathematical approach to evaluate through and cross coupling

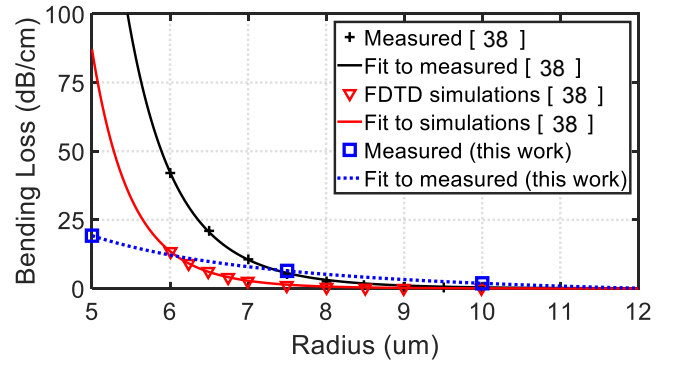


Fig. 14. Bending loss of ring resonators as a function of radius based on the simulations and measurements presented in [38] and measurements presented in this work.

coefficients (t and κ) in waveguide structures that include nonuniform coupling regions. The coupling strength can be obtained by evaluating Eq. (11) once modal coefficients (a_E , a_O , γ_E , γ_O) related to wavelengths and waveguide dimensions and materials have been derived. Note that the approach can be applied to more complicated structures than a circular ring coupled with a rectilinear waveguide, as developed in Appendix III and summarized in Fig. 4. In particular, structures involving a waveguide circularly shaped around a ring [4] can also be modeled as pictured in Fig. 13(a). Fig. 13(b) compares the cross coupling coefficient of a straight bus with the circular bus waveguide.

Finally, we point out that Eq. (11) presents the estimation of the coupling strength for the cases in which both structures (such as a ring and a bus waveguide) are made of identical waveguides. In cases where the width of the ring is not equal to the width of the waveguide, a clear definition of the curvature function is not possible. However, the coupling strength can still be approximated through the result of discretization of the coupling region by including the mode overlap factors [see also Appendix I]. Overall, the slight disagreement between our modeling approach and the FDTD results can be attributed to 1) the finite grid resolution for our optical mode database, 2) the inherent error in considering uniform coupling in small segments, and 3) mesh size in FDTD simulations.

IV. MODELING THE OPTICAL LOSS OF THE RING

The second compact model relates the loss inflicted to signals transiting inside the MRR to its size. The loss of the optical mode inside the ring has three contributors: 1) Loss due to the material absorption and surface state absorption, 2) scattering, mainly due to sidewall roughness and 3) radiation loss due to the curvature of the ring. The first contributor applies to any waveguide and is independent of the MRR radius. The last contributor radiation loss, in contrast, is widely characterized by the waveguide bending (and for this reason called bending loss). Scattering loss, finally, is present in straight waveguides but can be exacerbated in bent ones as the optical mode is shifted closer to the waveguide boundaries. Radiation loss has been extensively studied from a theoretical perspective [65], [66]. Numerical FDTD models have also been used to express the bending loss as a function of the ring radius [22], [38], [42]. However, none of these approaches can

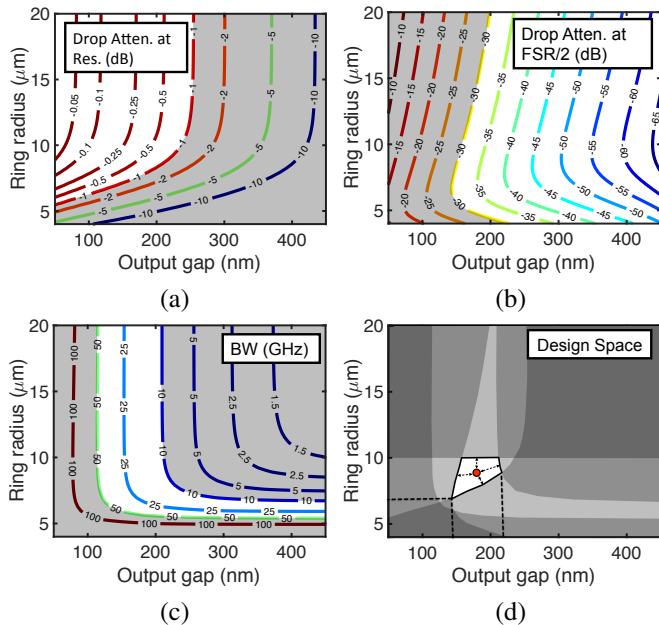


Fig. 15. Characterization of design space for microring Add-drop filters based on strip waveguides and the baseline loss model [38]. (a) Contours of attenuation at the resonance. The white area corresponds to less than 1 dB attenuation. (b) Contours of attenuation at half FSR. White area corresponds to attenuation better than 30 dB. (c) Contours of 3 dB optical bandwidth. White area corresponds to a bandwidth greater than 10 GHz and less than 50 GHz. (d) Overall design space of add-drop ring filters.

directly relate to fabrication defects, which play a major role in defining scattering losses.

Acknowledging that a method taking into account fabrication related imperfections is hard to construct, we consider the bending loss as a fabrication-platform dependent relationship, to be obtained experimentally and fitted. Such experimental measurements of the ring loss (compared to the loss of a straight waveguide) have been recently reported in [38]. We fitted these measurements with a power law

$$\alpha_{[dB/cm]} = a (R_{\mu m})^{-b} + c \quad (20)$$

where R is the ring radius (in micron units) and a , b and c are constant parameters. Hence, we assume the bending loss to be infinite for null radius and a constant for infinite radius (i.e. rectilinear waveguide). As shown in Fig. 14, the fit agrees reasonably well with two sets of measurements, one provided by authors of [38] (with parameters $a = 4.5323 \times 10^8$ and $b = 9.0334$, $c \approx 0$), the other collected from our fabricated structures (with parameters $a = 2096.3$, $b = 2.9123$, and $c = 0$). The power law fit is also in good agreement with FDTD simulations realized in [38] (with parameters $a = 1.1452 \times 10^9$ and $b = 10.1848$, $c = 0$). As indicated in [38], an additional radius-independent propagation loss must be added to the bending loss to include the effects of material absorption and standard sidewall roughness. Our baseline compact model for ring loss (black curve in Fig. 14) considers the aforementioned a and b values, plus a constant loss of $c = 2$ dB/cm [67]. Note that the rings studied in [38] are made of ridge waveguides with 90 nm of slab thickness while the rings in this work are made of strip waveguides.

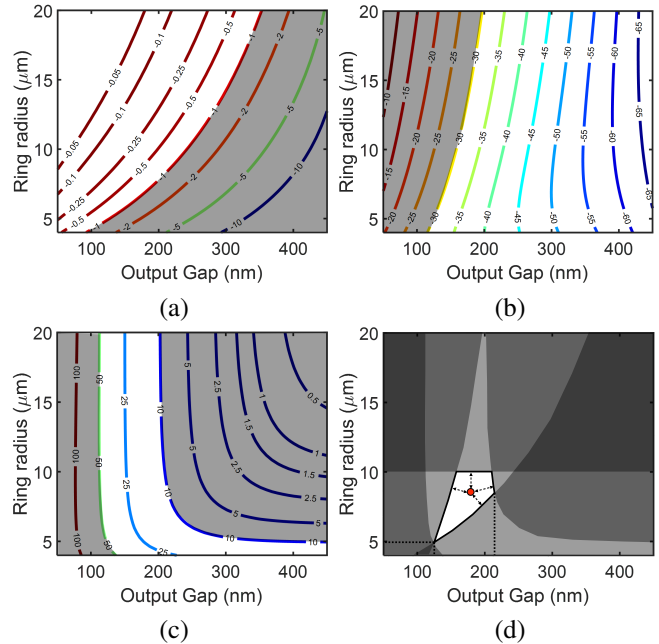


Fig. 16. Characterization of design space for microring Add-drop filters based on strip waveguides and the loss model from our direct measurements. (a) Contours of drop attenuation at the resonance. The white area corresponds to less than 1 dB attenuation. (b) Contours of attenuation at half FSR. White area corresponds to attenuation better than 30 dB. (c) Contours of 3 dB optical bandwidth. White area corresponds to a bandwidth greater than 10 GHz and less than 50 GHz. (d) Overall design space of add-drop ring filters.

V. DESIGN SPACE FOR ADD-DROP FILTERS

Add-Drop ring structures can serve as wavelength selective filters and demultiplexers for WDM-based optical links [33]. The design space for each individual ring can be constructed as shown in the plots of Fig. 15. The main assumptions that we apply are that the ring is made of 450×220 nm strip waveguides and is operating at critical coupling. This condition is satisfied when $t_{in}^2 = L \times t_{drp}^2$. For the loss of the ring, we use the power-law model that fits the measured ring losses in Fig. 14. Satisfaction of critical coupling condition requires that $\kappa_{drp} < \kappa_{in}$, and hence the drop gap (*output gap*) should be slightly bigger than the input gap. We take the output gap as the independent variable and find the input gap such that the critical coupling condition is held.

Since the design space depends on the loss of the ring, we consider two cases one of which is for the loss model fitted to measured data in [38] and the other one is for the loss model fitted to the data from our own measurements.

Fig. 15 shows the exploration of the design space for the first case. Fig. 15(a) shows the contours of drop insertion loss at the resonance. By limiting the insertion loss of the drop path to better than 1 dB, the design space is divided such that a larger radius is accompanied by a larger gap size. Fig. 15(b) describes the spectral attenuation of the drop path at FSR/2 detuning from the resonance. This is also describing the extinction of each resonance in the spectrum. We set the requirement for the extinction of resonance to be better than -30 dB to provide at least -20 dB crosstalk suppression in a WDM link [34]. Therefore, the left side of the design space is grayed out in Fig. 15(b). Fig. 15(c) shows the 3dB optical bandwidth of the drop filter. Considering a minimum signaling rate of 10Gbps-

per- λ for a WDM-based link, we require that the bandwidth of the filter be greater than 10 GHz yet less than 50 GHz, and gray out the undesired regions. Finally, we demand that each add-drop ring filter should provide a minimum FSR of 10 nm to allow at least 10×10 Gbps channels spaced 1 nm apart from each other. This sets the upper-bound of radius to about $10 \mu\text{m}$. The combination of all these constraints results in a design space, shown in Fig. 15(d), limiting the radius to $7 \mu\text{m} - 10 \mu\text{m}$ and the output gap to $150 \text{ nm} - 210 \text{ nm}$. The ideal design point is shown with a red circle on Fig. 15(d). This point is at the center of the design space corresponding to a radius of about $9 \mu\text{m}$ and output gap of 180 nm. This choice of design point will to some extent be immune to variations on the radius and gap size since the variations on the width of the waveguides are typically within 5 nm [48].

Fig. 16 shows the exploration of the design space for the second case. Same conditions are applied to constrain the design space in Fig. 16(a) for the drop loss at resonance, Fig. 16(b) for the extinction of resonance, and Fig. 16(c) for the 3 dB optical bandwidth of the ring. Fig. 16(d) shows the optimal design space for this case. Compared to the previous case, smaller radii (down to $5 \mu\text{m}$) are supported in the design space. The optimal design point in Fig. 16(d) is characterized by $8.6 \mu\text{m}$ radius and an output gap of 178 nm. As can be seen, the optimal point in this case is very close to the previous case even though the loss models were quite different for small radii.

VI. CONCLUSIONS

We introduced compact models for coupling coefficients and bending loss of ring resonators in SOI platform. The model for coupling coefficients was first validated by full-wave 3D FDTD simulations and then through direct measurements of spectral response of fabricated devices. The model for loss established a power-law relation between the loss of the ring and its radius. It was shown that this model can be reasonably well fitted to the measurements and simulated bending loss of ring resonators.

The proposed compact models were used to characterize a realistic design space for ring resonators that are performing as add-drop demultiplexers in WDM applications. It was concluded that the design space for add-drop ring filters results in a range of radii from $5 \mu\text{m}$ to $10 \mu\text{m}$ and gap sizes from 120 nm to 210 nm. The center point of the design space was chosen as the optimal design point whose radius is about $9 \mu\text{m}$, output gap is about 180 nm, and is operating at critical coupling. This design will provide better than 30 dB of extinction for the resonance, a drop loss less than 0.5 dB and a resonance bandwidth of about 20 GHz, with an FSR greater than 10 nm.

APPENDIX I

The schematic of a directional coupler made of two waveguides is shown in Fig. 17. Region 1 on the left side indicates the optical mode for $z < 0$ given by

$$\Psi_L(y, z) = a_1(z)\Psi_1(y) \exp(-j\beta_1 z) + a_2(z)\Psi_2(y) \exp(-j\beta_2 z) \quad (\text{A1})$$

where $\Psi_1(y)$ and $\Psi_2(y)$ are the individual modes of each waveguide and $a_1(z)$ and $a_2(z)$ correspond to the amplitudes. Region 2 in the middle indicates the coupling region in which the optical mode can be expressed as the superposition of the even, Ψ_e , and odd, Ψ_o , coupled supermodes:

$$\Psi_C(y, z) = A_e \Psi_e(y) \exp(-j\beta_e z) + A_o \Psi_o(y) \exp(-j\beta_o z). \quad (\text{A2})$$

Finally, region 3 on the right side indicates the optical mode for $z > l$ given by

$$\Psi_R(y, z) = a_1(z)\Psi_1(y) \exp(-j\beta_1(z-l)) + a_2(z)\Psi_2(y) \exp(-j\beta_2(z-l)). \quad (\text{A3})$$

In order to find the transfer matrix of this directional coupler that relates the amplitudes of the optical modes in regions 1 and 3, boundary conditions at $z = 0$ and $z = l$ must be satisfied. Applying the boundary condition at $z = 0$ and using the orthogonality property of the modes results in

$$\begin{pmatrix} A_e \\ A_o \end{pmatrix} = \mathbf{M} \times \begin{pmatrix} a_1(0) \\ a_2(0) \end{pmatrix} \quad (\text{A4})$$

where

$$\mathbf{M} = \begin{pmatrix} \langle \Psi_e | \Psi_1 \rangle & \langle \Psi_e | \Psi_2 \rangle \\ \langle \Psi_o | \Psi_1 \rangle & \langle \Psi_o | \Psi_2 \rangle \end{pmatrix}. \quad (\text{A5})$$

Applying the boundary condition at $z = l$ results in

$$\begin{pmatrix} A_e \\ A_o \end{pmatrix} = \mathbf{E}^{-1} \times \mathbf{M} \times \begin{pmatrix} a_1(l) \\ a_2(l) \end{pmatrix} \quad (\text{A6})$$

where

$$\mathbf{E} = \begin{pmatrix} \exp(-j\beta_e l) & 0 \\ 0 & \exp(-j\beta_o l) \end{pmatrix}. \quad (\text{A7})$$

Combining equations (A4)-(A7) finally leads to the transfer matrix of the directional coupler:

$$\begin{pmatrix} a_1(l) \\ a_2(l) \end{pmatrix} = (\mathbf{M}^{-1} \mathbf{E} \mathbf{M}) \times \begin{pmatrix} a_1(0) \\ a_2(0) \end{pmatrix}. \quad (\text{A8})$$

In order to reach the expression presented in Eq. (4), we examine the case of coupling of two identical waveguides. By considering the normalization for the coupled supermodes

$$\langle \Psi_e | \Psi_e \rangle = 1, \quad \langle \Psi_o | \Psi_o \rangle = 1 \quad (\text{A9})$$

and the optical mode profiles plotted on Fig. 17, the following relations can be concluded:

$$\langle \Psi_e | \Psi_1 \rangle \approx \langle \Psi_e | \Psi_2 \rangle \quad (\text{A10})$$

$$\langle \Psi_o | \Psi_1 \rangle \approx -\langle \Psi_o | \Psi_2 \rangle. \quad (\text{A11})$$

This leads to the transfer matrix given by

$$\mathbf{M}^{-1} \mathbf{E} \mathbf{M} \approx \exp(-j\beta_+ l) \begin{pmatrix} \cos(\beta_- l) & -j \sin(\beta_- l) \\ -j \sin(\beta_- l) & \cos(\beta_- l) \end{pmatrix} \quad (\text{A12})$$

where

$$\beta_+ = (\beta_e + \beta_o)/2, \quad (\text{A13})$$

$$\beta_- = (\beta_e - \beta_o)/2. \quad (\text{A14})$$

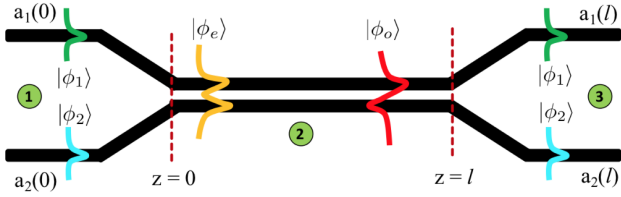


Fig. 17. Structure of a directional coupler. The coupling region has two supermodes (Ψ_e for the even mode, Ψ_o for the odd mode). The transfer matrix relates the amplitudes of the optical modes at $z = 0$ and $z = l$.

APPENDIX II

In order to derive Eq. (11) we begin by remarking that for an identical pair of coupled waveguides, the effective index of the supermodes can be accurately fitted by exponential curves as a function of gap sizes given by

$$n_E \approx n_{\text{eff}} + a_E \exp(-\gamma_E g) \quad (\text{A15})$$

for the even mode, and

$$n_O \approx n_{\text{eff}} - a_O \exp(-\gamma_O g) \quad (\text{A16})$$

for the odd mode, where g is the coupling gap size between the two waveguides and n_{eff} is the effective index of the uncoupled waveguide. For a given width and height of the waveguides, the four fitting parameters $a_E, a_O, \gamma_E, \gamma_O$ are positive and only depend on the wavelength. The values for these parameters are provided in Table 1 for 400×220 nm, 450×220 nm, and 500×220 nm strip waveguides. Fig. 18(a) shows the fitting of these exponential curves for 400×220 nm strip waveguides at 1550 nm wavelength. As can be observed, the exponential fits can closely match the numerical values of the effective indices. Using these two exponential fittings, we can then turn Eq. 10(b) into an integral form and write κ as

$$\kappa = \sin \left(\frac{\pi}{\lambda} \int_{z_{\min}}^{z_{\max}} [n_E(z) - n_O(z)] dz \right) \quad (\text{A17})$$

where $Z_{\min} = -Z_{\max}$ due to the symmetry. In order to calculate the integral, the gap must be expressed as a function of z . It is easier to use polar coordinates where

$$z = (R + w/2) \sin(\theta), \quad (\text{A18})$$

$$g(z) = d + (R + w/2)(1 - \cos(\theta)), \quad (\text{A19})$$

$$z_{\max} = (R + w/2) \sin(\theta_0), \quad (\text{A20})$$

and θ_0 is the angle that corresponds to the maximum coupling distance between the ring and the waveguide [see Fig. 18(b)]. It can be calculated by

$$\theta_0 = \cos^{-1} \left(1 - \frac{D - d}{R + w/2} \right). \quad (\text{A21})$$

Using the above equations, the integral in (A17) is reduced to

$$\begin{aligned} & \int_{z_{\min}}^{z_{\max}} [n_E(z) - n_O(z)] dz = \\ & 2 \frac{a_E x_E}{\gamma_E} e^{-\gamma_E d} \int_0^{\theta_0} e^{-x_E(1 - \cos(\theta))} \cos(\theta) d\theta + \\ & 2 \frac{a_O x_O}{\gamma_O} e^{-\gamma_O d} \int_0^{\theta_0} e^{-x_O(1 - \cos(\theta))} \cos(\theta) d\theta \quad (\text{A22}) \end{aligned}$$

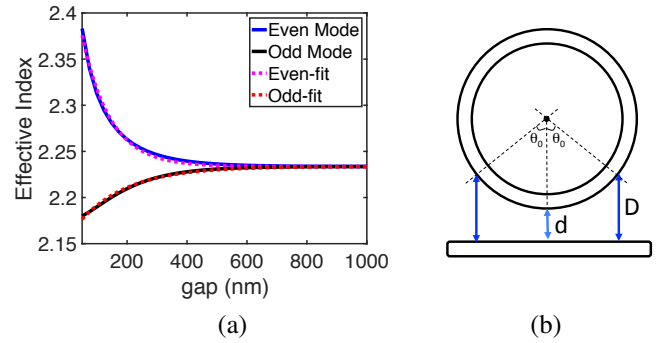


Fig. 18. (a) Exponential fitting of the effective index of the even and odd supermodes for two identical 400×220 nm strip waveguides as a function of coupling gap size. (b) Ring-waveguide coupling structure. D is the maximum distance that coupling occurs between the ring and the waveguide and θ_0 is the maximum angle. In the limit, $\theta_0 \rightarrow \pi/2$ and $D \rightarrow R + d + w/2$.

where we defined $x_{E,O} = \gamma_{E,O}(R + w/2)$. The two integrals in the above equations are values of the function $F(x, \phi)$ defined by

$$F(x, \phi) = \int_0^\phi \exp(-x(1 - \cos \theta)) \cos(\theta) d\theta. \quad (\text{A23})$$

Finally, we note that in the limit the coupling between the ring and the waveguide can go all the way to the side edges of the ring, i.e. $D \rightarrow d + R + w/2$ which results in $\theta_0 \rightarrow \pi/2$. In that case by defining $B(x) = 2x F(x, \pi/2)$, Eq. (12) and Eq. (13) are obtained.

APPENDIX III

As we pointed out in Section III-A, Eq. (11) can be viewed as a general equation that can estimate the coupling between two identical waveguides with any arbitrary coupling region. The curvature and nonuniformity of the coupling region is entirely lumped inside the curvature function $B(x)$. Here we extend our analysis of the ring-waveguide coupling to provide the curvature function $B(x)$ for different types of coupling structures.

A. Two Straight Waveguides

For two identical straight waveguides of length L coupled to each other (Fig. 4), the gap is constant

$$g(z) = d \quad (\text{A24})$$

and the curvature function is given by

$$B(x) = x \quad (\text{A25})$$

where $x_{E,O} = \gamma_{E,O}L$.

B. Directional Coupler with S-bends

S-bends are usually used to bring two straight waveguides close to each other in the coupling region and then taking them away from each other (Fig. 4). S-bends are parametrically defined by a cosine function

$$Z(t) = Ht, Y(t) = \frac{V}{2}(1 - \cos(\pi t)) \quad (\text{A26})$$

where $0 < t < 1$ is the parameter of the curve, H is the horizontal offset of the S-bend and V is the vertical offset. In this case, the gap is given by

$$g(z) = \begin{cases} d & |z| \leq L/2 \\ d + V(1 - \cos(\pi \frac{|z| - L/2}{H})) & L/2 \leq |z| \leq L/2 + H \end{cases} \quad (\text{A27})$$

and the curvature function is calculated as

$$B(x) = x \left[1 + \frac{2H}{L} \exp(-Vx/L) I_0(Vx/L) \right] \quad (\text{A28})$$

where $x_{E,O} = \gamma_{E,O}L$. Here, $I_0(x)$ is the modified Bessel function of the first kind of order zero.

C. Ring-Ring Coupling

In the case of two identical ring resonators coupled to each other as shown in Fig. 4, the curvature function is given by

$$B_{\text{Ring-Ring}}(x) = 0.5 B_{\text{Ring-wg}}(2x) \quad (\text{A29})$$

where $x_{E,O} = \gamma_{E,O}(R + w/2)$. It can be easily verified that the $B(x)$ function for ring-ring coupling is always smaller than the $B(x)$ function for the ring-waveguide coupling. More precisely, based on the approximation of $B_{\text{Ring-wg}}(x) \approx \sqrt{2}\pi x$, it can be seen that

$$\frac{B_{\text{Ring-Ring}}(x)}{B_{\text{Ring-wg}}(x)} \approx \frac{1}{\sqrt{2}} = 0.71 \quad (\text{A30})$$

for large values of x . Considering that $a_E, a_O, \gamma_E, \gamma_O$ in Eq. (11) do not depend on the curvature of the coupling region, (A30) results in the following relation

$$\frac{\kappa_{\text{Ring-Ring}}}{\kappa_{\text{Ring-wg}}} \approx \frac{1}{\sqrt{2}} = 0.71 \quad (\text{A31})$$

To show this, we performed an FDTD simulation in RSoft software [68] for 400×220 nm strip waveguides and $5 \mu\text{m}$ radius of curvature. The calculated power couplings (κ^2) are plotted in Fig. 19. A good agreement is observed.

D. Race-track ring structure

For the case of a race-track ring structure as shown in Fig. 4, the gap function is given by

$$g(z) = \begin{cases} d & |z| \leq L/2 \\ d + (R + w/2)(1 - \cos \theta) & L/2 \leq |z| \end{cases} \quad (\text{A32})$$

and the curvature function is calculated as

$$B_{\text{Race-track}}(x) = \frac{L}{R + w/2} x + B_{\text{Ring-wg}}(x) \quad (\text{A33})$$

where $x_{E,O} = \gamma_{E,O}(R + w/2)$. Note that in general, the curvature function of the race-track structure can be written as a superposition of the curvature functions of waveguide-waveguide and ring-waveguide structures

$$B_{\text{Race-track}} = B_{\text{wg-wg}}(x_{\text{wg}}) + B_{\text{Ring-wg}}(x_{\text{ring}}) \quad (\text{A34})$$

where $x_{\text{wg}} = \gamma L$ and $x_{\text{ring}} = \gamma(R + w/2)$ for even and odd modes.

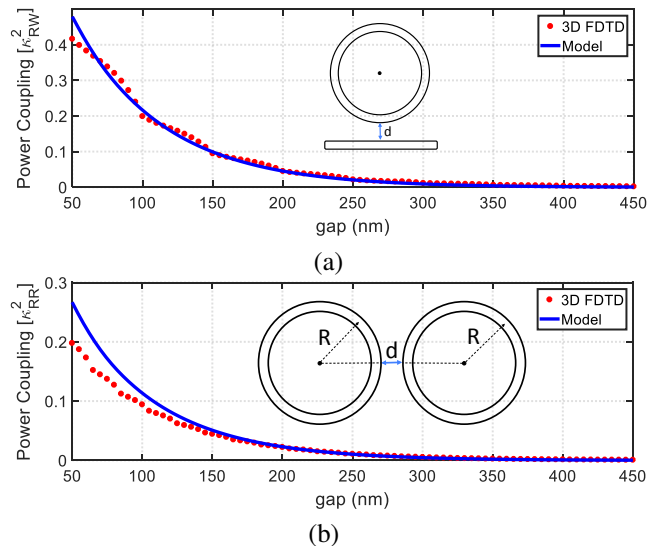


Fig. 19. (a) Plot of the ring-waveguide power coupling (κ_{RW}^2) for 400×220 nm strip waveguides and $5 \mu\text{m}$ radius. Solid blue curve is estimated from our model and circles are from a 3D FDTD simulation (RSoft). (b) Plot of the ring-ring power coupling coefficient (κ_{RR}^2) for 400×220 nm strip waveguides and $5 \mu\text{m}$ radius. Solid blue curve is estimated from our model and circles are from a 3D FDTD simulation (RSoft). The ratio between case (a) and case (b) is close to 2 as predicted by our model.

E. Ring resonator with circularly shaped bus waveguide

In this case as shown in Fig. 4, the bus waveguide has a circular part around the ring over an angle of θ_0 . This makes the coupling region approximately a uniform region whose gap function is $g(z) = d$ and the curvature function is given by $B(x) \approx x$ where $x_{E,O} = \gamma_{E,O}(R + w/2 + d/2)$. Fig. 13(b) shows a comparison between the coupling of a ring resonator to a straight waveguide and the coupling of a ring to a circularly shaped waveguide (based on 400×220 nm strip waveguides and a radius of $5 \mu\text{m}$).

APPENDIX IV

Considering the compact model presented in Fig. 12(b) with the lumped reflector characterized by a transmittance t and reflectance $r = \sqrt{1 - t^2}$ inside the ring, the scattering parameter from the input port (port 1) to the drop port (port 4) is given by

$$S_{41} = (-\kappa_1 \kappa_2 L^{0.25} \exp(-j\phi/2)) \frac{t - O}{1 - 2tO + O^2} \quad (\text{A35})$$

where ϕ is the round-trip phase inside the ring, O is the loop gain of the ring given by

$$O = t_1 t_2 \sqrt{L} \exp(-j\phi). \quad (\text{A36})$$

$\kappa_1, \kappa_2, t_1, t_2$ are the coefficients of the input and output couplers (DC1 and DC2) and L is the round-trip power attenuation inside the ring without a reflector. The splitting of the resonance into two peaks can be characterized by defining $t = \cos(\phi_t)$ and then

$$\frac{t - O}{1 - 2tO + O^2} = -\frac{1}{2} \left(\frac{1}{O - e^{j\phi_t}} + \frac{1}{O - e^{-j\phi_t}} \right). \quad (\text{A37})$$

By expanding the round-trip phase around the resonance frequency as

$$\phi(\omega) = 2\pi R \left(\beta(\omega_0) + \frac{d\beta}{d\omega}(\omega - \omega_0) \right), \quad (\text{A38})$$

Eq. (A37) is given as the sum of two Lorentzian terms:

$$\frac{t - O}{1 - 2tO + O^2} = \frac{A}{2} \left(\frac{1}{(\omega - \omega_+) + \frac{\Delta\omega_0}{2}} + \frac{1}{(\omega - \omega_-) + \frac{\Delta\omega_0}{2}} \right). \quad (\text{A39})$$

where $A = FSR/\xi$ and $\Delta\omega_0$ is the original 3 dB bandwidth of the ring without the reflector. The frequencies of the two peaks are given by

$$\omega_{\pm} = \omega_0 \pm \frac{FSR}{\xi} \sqrt{1 - t^2}. \quad (\text{A40})$$

ACKNOWLEDGMENTS

This work is supported in part by Air Force Research Laboratory under agreement number FA8650-15-2-5220, and by the US Department of Energy (DoE) under government subcontract number B621301. Authors also acknowledge support from NSF under E2CDA grant agreement number CCF-1640108, and from SRC under the grant number SRS 2016-EP-2693-A.

REFERENCES

[1] M. Pantouvaki, S. Srinivasan, Y. Ban, P. De Heyn, P. Verheyen, G. Lepage, H. Chen, J. De Coster, N. Golshani, S. Balakrishnan *et al.*, "Active components for 50 gb/s nrz-ook optical interconnects in a silicon photonics platform," *Journal of Lightwave Technology*, vol. 35, no. 4, pp. 631–638, 2017.

[2] C. Sun, M. T. Wade, Y. Lee, J. S. Orcutt, L. Alloatti, M. S. Georgas, A. S. Waterman, J. M. Shainline, R. R. Avizienis, S. Lin *et al.*, "Single-chip microprocessor that communicates directly using light," *Nature*, vol. 528, no. 7583, pp. 534–538, 2015.

[3] J. E. Cunningham, I. Shubin, X. Zheng, T. Pinguet, A. Mekis, Y. Luo, H. Thacker, G. Li, J. Yao, K. Raj *et al.*, "Highly-efficient thermally-tuned resonant optical filters," *Optics Express*, vol. 18, no. 18, pp. 19055–19063, 2010.

[4] C. Manganelli, P. Pintus, F. Gambini, D. Fowler, M. Fournier, S. Faralli, C. Kopp, and C. Oton, "Large-fsr thermally tunable double-ring filters for wdm applications in silicon photonics," *IEEE Photonics Journal*, vol. 9, no. 1, pp. 1–10, 2017.

[5] S. Xiao, M. H. Khan, H. Shen, and M. Qi, "Multiple-channel silicon micro-resonator based filters for wdm applications," *Optics Express*, vol. 15, no. 12, pp. 7489–7498, 2007.

[6] S. Palermoa, K. Yua, A. Roshan-Zamira, B. Wangb, C. Lib, M. A. Seyedib, M. Fiorentinob, and R. Beausoleilb, "Pam4 silicon photonic microring resonator-based transceiver circuits," in *Proc. of SPIE Vol.*, vol. 10109, 2017, pp. 101 090F–1.

[7] G. Li, X. Zheng, J. Yao, H. Thacker, I. Shubin, Y. Luo, K. Raj, J. E. Cunningham, and A. V. Krishnamoorthy, "25gb/s 1v-driving cmos ring modulator with integrated thermal tuning," *Optics Express*, vol. 19, no. 21, pp. 20435–20443, 2011.

[8] M. A. Popović, T. Barwicz, M. R. Watts, P. T. Rakich, L. Socci, E. P. Ippen, F. X. Kärtner, and H. I. Smith, "Multistage high-order microring-resonator add-drop filters," *Optics letters*, vol. 31, no. 17, pp. 2571–2573, 2006.

[9] P. Dong, S. F. Preble, and M. Lipson, "All-optical compact silicon comb switch," *Optics express*, vol. 15, no. 15, pp. 9600–9605, 2007.

[10] A. Biberman, H. L. Lira, K. Padmaraju, N. Ophir, M. Lipson, and K. Bergman, "Broadband cmos-compatible silicon photonic electro-optic switch for photonic networks-on-chip," in *Conference on Lasers and Electro-Optics*. Optical Society of America, 2010, p. CPDA11.

[11] H. Subbaraman, X. Xu, A. Hosseini, X. Zhang, Y. Zhang, D. Kwong, and R. T. Chen, "Recent advances in silicon-based passive and active optical interconnects," *Optics express*, vol. 23, no. 3, pp. 2487–2511, 2015.

[12] A. E.-J. Lim, J. Song, Q. Fang, C. Li, X. Tu, N. Duan, K. K. Chen, R. P.-C. Tern, and T.-Y. Liow, "Review of silicon photonics foundry efforts," *IEEE Journal of Selected Topics in Quantum Electronics*, vol. 20, no. 4, pp. 405–416, 2014.

[13] B. Wang, C. Li, C.-H. Chen, K. Yu, M. Fiorentino, R. G. Beausoleil, and S. Palermo, "A compact verilog-a model of silicon carrier-injection ring modulators for optical interconnect transceiver circuit design," *Journal of Lightwave Technology*, vol. 34, no. 12, pp. 2996–3005, 2016.

[14] J. Komma, C. Schwarz, G. Hofmann, D. Heinert, and R. Nawrodt, "Thermo-optic coefficient of silicon at 1550 nm and cryogenic temperatures," *Applied Physics Letters*, vol. 101, no. 4, p. 041905, 2012.

[15] K. Padmaraju and K. Bergman, "Resolving the thermal challenges for silicon microring resonator devices," *Nanophotonics*, vol. 3, no. 4-5, pp. 269–281, 2014.

[16] F. Gan, T. Barwicz, M. Popovic, M. Dahlem, C. Holzwarth, P. Rakich, H. Smith, E. Ippen, and F. Kartner, "Maximizing the thermo-optic tuning range of silicon photonic structures," in *Photonics in Switching, 2007*. IEEE, 2007, pp. 67–68.

[17] A. Masood, M. Pantouvaki, G. Lepage, P. Verheyen, J. Van Campenhout, P. Absil, D. Van Thourhout, and W. Bogaerts, "Comparison of heater architectures for thermal control of silicon photonic circuits," in *Group IV Photonics (GFP), 2013 IEEE 10th International Conference on*. IEEE, 2013, pp. 83–84.

[18] A. Gazman, C. Browning, M. Bahadori, Z. Zhu, P. Samadi, S. Rumley, V. Vujicic, L. P. Barry, and K. Bergman, "Software-defined control-plane for wavelength selective unicast and multicast of optical data in a silicon photonic platform," *Optics express*, vol. 25, no. 1, pp. 232–242, 2017.

[19] K. Padmaraju, D. F. Logan, T. Shiraishi, J. J. Ackert, A. P. Knights, and K. Bergman, "Wavelength locking and thermally stabilizing microring resonators using dithering signals," *Journal of Lightwave Technology*, vol. 32, no. 3, pp. 505–512, 2014.

[20] M. Nedeljkovic, S. Stankovic, C. J. Mitchell, A. Z. Khokhar, S. A. Reynolds, D. J. Thomson, F. Y. Gardes, C. G. Littlejohns, G. T. Reed, and G. Z. Mashanovich, "Mid-infrared thermo-optic modulators in soi," *IEEE Photon. Technol. Lett.*, vol. 26, no. 13, pp. 1352–1355, 2014.

[21] M. R. Watts, J. Sun, C. DeRose, D. C. Trotter, R. W. Young, and G. N. Nielson, "Adiabatic thermo-optic mach-zehnder switch," *Optics letters*, vol. 38, no. 5, pp. 733–735, 2013.

[22] C. Li, W. Zheng, P. Dang, C. Zheng, Y. Wang, and D. Zhang, "Silicon-microring-based thermo-optic non-blocking four-port optical router for optical networks-on-chip," *Optical and Quantum Electronics*, vol. 48, no. 12, p. 552, 2016.

[23] O. Dubray, A. Abraham, K. Hassan, S. Olivier, D. Marris-Morini, L. Vivien, I. O'Connor, and S. Menezo, "Electro-optical ring modulator: An ultracompact model for the comparison and optimization of pn, pin, and capacitive junction," *IEEE Journal of Selected Topics in Quantum Electronics*, vol. 22, no. 6, pp. 89–98, 2016.

[24] P. Dong, S. Liao, H. Liang, W. Qian, X. Wang, R. Shafiq, D. Feng, G. Li, X. Zheng, A. V. Krishnamoorthy *et al.*, "High-speed and compact silicon modulator based on a racetrack resonator with a 1 v drive voltage," *Optics letters*, vol. 35, no. 19, pp. 3246–3248, 2010.

[25] F. Y. Liu, D. Patil, J. Lexau, P. Amberg, M. Dayringer, J. Gainsley, H. F. Moghadam, X. Zheng, J. E. Cunningham, A. V. Krishnamoorthy *et al.*, "10-Gbps, 5.3-mW optical transmitter and receiver circuits in 40-nm CMOS," *IEEE Journal of Solid-State Circuits*, vol. 47, no. 9, pp. 2049–2067, 2012.

[26] K. Yu, C.-H. Chen, A. Titriku, A. Shafik, M. Fiorentino, P. Y. Chiang, S. Palermo *et al.*, "25gb/s hybrid-integrated silicon photonic receiver with microring wavelength stabilization," in *Optical Fiber Communication Conference*. Optical Society of America, 2015, pp. W3A–6.

[27] R. Ding, Y. Liu, Q. Li, Z. Xuan, Y. Ma, Y. Yang, A. E.-J. Lim, G.-Q. Lo, K. Bergman, T. Baehr-Jones *et al.*, "A compact low-power 320-gb/s wdm transmitter based on silicon microrings," *IEEE Photonics Journal*, vol. 6, no. 3, pp. 1–8, 2014.

[28] S. Faralli, N. Andriolli, F. Gambini, P. Pintus, G. Preve, M. Chiesa, R. Ortuño, O. Liboiron-Ladouceur, and I. Cerutti, "Bidirectional transmissions in a ring-based packaged optical noc with 12 add-drop microrings," in *Photonics Conference (IPC), 2016 IEEE*. IEEE, 2016, pp. 621–622.

[29] F. Gambini, P. Pintus, S. Faralli, M. Chiesa, G. B. Preve, I. Cerutti, and N. Andriolli, "Experimental demonstration of a 24-port packaged multi-microring network-on-chip in silicon photonic platform," *Optics Express*, vol. 25, no. 18, pp. 22004–22016, 2017.

[30] S. V. R. Chittamuru, I. G. Thakkar, and S. Pasricha, "Hydra: Heterodyne crosstalk mitigation with double microring resonators and data encoding for photonic nocs," *IEEE Transactions on Very Large Scale Integration (VLSI) Systems*, 2017.

- [31] F. G. de Magalhaes, F. Hessel, O. Liboiron-Ladouceur, and G. Nicolescu, "Modelling and simulation of optical integrated networks for early-stage design exploration (wip)," in *SummerSim*, 2016, p. 44.
- [32] M. Bahadori, S. Rumley, R. Polster, A. Gazman, M. Traverso, M. Webster, K. Patel, and K. Bergman, "Energy-performance optimized design of silicon photonic interconnection networks for high-performance computing," in *2017 Design, Automation & Test in Europe Conference & Exhibition (DATE)*. IEEE, 2017, pp. 326–331.
- [33] M. Bahadori, S. Rumley, D. Nikolova, and K. Bergman, "Comprehensive design space exploration of silicon photonic interconnects," *Journal of Lightwave Technology*, vol. 34, no. 12, pp. 2975–2987, 2016.
- [34] M. Bahadori, S. Rumley, H. Jayatilleka, K. Murray, N. A. Jaeger, L. Chrostowski, S. Shekhar, and K. Bergman, "Crosstalk penalty in microring-based silicon photonic interconnect systems," *Journal of Lightwave Technology*, vol. 34, no. 17, pp. 4043–4052, 2016.
- [35] D. Nikolova, S. Rumley, D. Calhoun, Q. Li, R. Hendry, P. Samadi, and K. Bergman, "Scaling silicon photonic switch fabrics for data center interconnection networks," *Optics express*, vol. 23, no. 2, pp. 1159–1175, 2015.
- [36] W. Bogaerts, P. De Heyn, T. Van Vaerenbergh, K. De Vos, S. Kumar Selvaraja, T. Claes, P. Dumon, P. Bienstman, D. Van Thourhout, and R. Baets, "Silicon microring resonators," *Laser & Photonics Reviews*, vol. 6, no. 1, pp. 47–73, 2012.
- [37] Y. Xie, M. Nikdast, J. Xu, W. Zhang, Q. Li, X. Wu, Y. Ye, X. Wang, and W. Liu, "Crosstalk noise and bit error rate analysis for optical network-on-chip," in *Proceedings of the 47th Design Automation Conference*. ACM, 2010, pp. 657–660.
- [38] H. Jayatilleka, M. Caverley, N. A. Jaeger, S. Shekhar, and L. Chrostowski, "Crosstalk limitations of microring-resonator based wdm demultiplexers on soi," in *Optical Interconnects Conference (OI), 2015 IEEE*. IEEE, 2015, pp. 48–49.
- [39] M. Nikdast, J. Xu, L. H. K. Duong, X. Wu, X. Wang, Z. Wang, Z. Wang, P. Yang, Y. Ye, and Q. Hao, "Crosstalk noise in wdm-based optical networks-on-chip: A formal study and comparison," *IEEE Transactions on Very Large Scale Integration (VLSI) Systems*, vol. 23, no. 11, pp. 2552–2565, 2015.
- [40] G. Li, A. V. Krishnamoorthy, I. Shubin, J. Yao, Y. Luo, H. Thacker, X. Zheng, K. Raj, and J. E. Cunningham, "Ring resonator modulators in silicon for interchip photonic links," *IEEE Journal of Selected Topics in Quantum Electronics*, vol. 19, no. 6, pp. 95–113, 2013.
- [41] R. Marchetti, V. Vitali, C. Lacava, I. Cristiani, G. Giuliani, V. Muffato, M. Fournier, S. Abrate, R. Gaudino, E. Temporiti *et al.*, "Low-loss micro-resonator filters fabricated in silicon by cmos-compatible lithographic techniques: design and characterization," *Applied Sciences*, vol. 7, no. 2, p. 174, 2017.
- [42] H. P. Bazargani, J. Azaña, L. Chrostowski, and J. Flueckiger, "Microring resonator design with improved quality factors using quarter bezier curves," in *CLEO: Applications and Technology*. Optical Society of America, 2015, pp. JTu5A–58.
- [43] K. Kakiyama, N. Kono, K. Saitoh, and M. Koshiba, "Full-vectorial finite element method in a cylindrical coordinate system for loss analysis of photonic wire bends," *Optics express*, vol. 14, no. 23, pp. 11 128–11 141, 2006.
- [44] P. Pintus, M.-C. Tien, and J. E. Bowers, "Design of magneto-optical ring isolator on soi based on the finite-element method," *IEEE Photonics Technology Letters*, vol. 23, no. 22, pp. 1670–1672, 2011.
- [45] J. C. Mak, W. D. Sacher, T. Xue, J. C. Mikkelsen, Z. Yong, and J. K. Poon, "Automatic resonance alignment of high-order microring filters," *IEEE Journal of Quantum Electronics*, vol. 51, no. 11, pp. 1–11, 2015.
- [46] B. E. Little, S. T. Chu, H. A. Haus, J. Foresi, and J.-P. Laine, "Microring resonator channel dropping filters," *Journal of lightwave technology*, vol. 15, no. 6, pp. 998–1005, 1997.
- [47] M. Nikdast, G. Nicolescu, J. Trajkovic, and O. Liboiron-Ladouceur, "Chip-scale silicon photonic interconnects: a formal study on fabrication non-uniformity," *Journal of Lightwave Technology*, vol. 34, no. 16, pp. 3682–3695, 2016.
- [48] P. Le Maître, J.-F. Carpentier, C. Baudot, N. Vulliet, A. Souhailé, J.-B. Quéléne, T. Ferrotti, and F. Bœuf, "Impact of process variability of active ring resonators in a 300nm silicon photonic platform," in *Optical Communication (ECOC), 2015 European Conference on*. IEEE, 2015, pp. 1–3.
- [49] Z. Lu, J. Jhoja, J. Klein, X. Wang, A. Liu, J. Flueckiger, J. Pond, and L. Chrostowski, "Performance prediction for silicon photonics integrated circuits with layout-dependent correlated manufacturing variability," *Optics Express*, vol. 25, no. 9, pp. 9712–9733, 2017.
- [50] <https://www.comsol.com/>. [Online]. Available: <https://www.comsol.com/>
- [51] B. E. Saleh, M. C. Teich, and B. E. Saleh, *Fundamentals of photonics*. Wiley New York, 1991, vol. 22.
- [52] G. Calò, A. D’Orazio, and V. Petruzzelli, "Broadband mach-zehnder switch for photonic networks on chip," *Journal of Lightwave Technology*, vol. 30, no. 7, pp. 944–952, 2012.
- [53] <http://www.aimphotonics.com/>. [Online]. Available: <http://www.aimphotonics.com/>
- [54] N. Dupuis, B. G. Lee, A. V. Rylakov, D. M. Kuchta, C. W. Baks, J. S. Orcutt, D. M. Gill, W. M. Green, and C. L. Schow, "Design and fabrication of low-insertion-loss and low-crosstalk broadband 2×2 mach-zehnder silicon photonic switches," *Journal of Lightwave Technology*, vol. 33, no. 17, pp. 3597–3606, 2015.
- [55] P. De Heyn, "Receivers based on silicon ring resonators for multi-wavelength optical interconnects," Ph.D. dissertation, Ghent University, 2014.
- [56] <https://optiwave.com/optiftd-overview/>. [Online]. Available: <https://optiwave.com/optiftd-overview/>
- [57] <https://www.lumerical.com/tcad-products/fdtd/>. [Online]. Available: <https://www.lumerical.com/tcad-products/fdtd/>
- [58] <http://gdsfy.readthedocs.io>. [Online]. Available: <http://gdsfy.readthedocs.io>
- [59] W. McKinnon, D.-X. Xu, C. Storey, E. Post, A. Densmore, A. Delâge, P. Waldron, J. Schmid, and S. Janz, "Extracting coupling and loss coefficients from a ring resonator," *Optics express*, vol. 17, no. 21, pp. 18 971–18 982, 2009.
- [60] B. E. Little, J.-P. Laine, and S. T. Chu, "Surface-roughness-induced contradiirectional coupling in ring and disk resonators," *Optics letters*, vol. 22, no. 1, pp. 4–6, 1997.
- [61] A. Li and W. Bogaerts, "Fundamental suppression of backscattering in silicon microrings," *Optics Express*, vol. 25, no. 3, pp. 2092–2099, 2017.
- [62] F. Morichetti, A. Canciamilla, M. Martinelli, A. Samarelli, R. De La Rue, M. Sorel, and A. Melloni, "Coherent backscattering in optical microring resonators," *Applied Physics Letters*, vol. 96, no. 8, p. 081112, 2010.
- [63] F. Morichetti, A. Canciamilla, C. Ferrari, M. Torregiani, A. Melloni, and M. Martinelli, "Roughness induced backscattering in optical silicon waveguides," *Physical review letters*, vol. 104, no. 3, p. 033902, 2010.
- [64] A. Li, T. Vaerenbergh, P. Heyn, P. Bienstman, and W. Bogaerts, "Backscattering in silicon microring resonators: a quantitative analysis," *Laser & Photonics Reviews*, vol. 10, no. 3, pp. 420–431, 2016.
- [65] F. Kapron, D. Keck, and R. Maurer, "Radiation losses in glass optical waveguides," *Applied Physics Letters*, vol. 17, no. 10, pp. 423–425, 1970.
- [66] H. Renner, "Bending losses of coated single-mode fibers: a simple approach," *Journal of Lightwave Technology*, vol. 10, no. 5, pp. 544–551, 1992.
- [67] T. Alasaarela, D. Korn, L. Alloati, A. Säynätjoki, A. Tervonen, R. Palmer, J. Leuthold, W. Freude, and S. Honkanen, "Reduced propagation loss in silicon strip and slot waveguides coated by atomic layer deposition," *Optics express*, vol. 19, no. 12, pp. 11 529–11 538, 2011.
- [68] <https://www.synopsys.com/optical-solutions/rsoft.html>. [Online]. Available: <https://www.synopsys.com/optical-solutions/rsoft.html>

Meisam Bahadori received his B.Sc. degree in electrical engineering, majoring in Communication Systems, with honors from Sharif University of Technology in 2011. After that, he worked toward M.Sc. degree in electrical engineering, majoring in Microwaves and Optics, at the same school and graduated with the highest honors in June 2013.

From fall 2011 to spring 2014, he worked as a research assistant at the Integrated Photonics Laboratory at Sharif University of Technology. He joined the Lightwave Research Laboratory at Columbia University in fall 2014 where he is currently pursuing a PhD degree in Electrical Engineering with a focus on Silicon Photonics. His current research interests include silicon photonic devices and nano-photonics.

Mahdi Nikdast (S'10-M'14) received his Ph.D. degree in Electronic and Computer Engineering from The Hong Kong University of Science and Technology, Hong Kong, in 2013. From 2014 to 2017, he was a Postdoctoral Fellow under The Silicon Electronic-Photonic Integrated Circuits (Si-EPIC) Program at Polytechnique Montréal and in collaboration with McGill University in Montréal, QC, Canada. In September 2017, Dr. Nikdast joined the Department of Electrical and Computer Engineering at Colorado State University, CO, USA as an Assistant Professor. He is the director of Emerging Computing Systems and Design Automation (ECSyD) Lab at CSU. His research interests include silicon photonics, high performance computing systems, interconnection networks, and system modeling and simulation.

Sébastien Rumley received his Ph.D. degree (in communication system) from EPFL, Switzerland, in 2011. He is currently Research Scientist in the Lightwave Research Laboratory led by Prof. Keren Bergman, Columbia University, New York. His research focuses on cross-scale modeling and optimization of large-scale interconnection networks, with particular focus on optical technologies and silicon photonics.

Liang Yuan Dai received his Bachelor of Engineering from New Jersey's Institute of Technology. He is currently a Ph.D. candidate working with the Lightwave Research Laboratory at Columbia University, directed by Dr. Keren Bergman. His research focus includes silicon device testing and packaging.

Natalie Janosik is currently a graduate student in the Lightwave Research Laboratory at Columbia University working for Dr. Keren Bergman. She is working towards her MS/PhD in Electrical Engineering focusing on Silicon Photonics. Her current research interests include optical computing and the use of nanotechnology for next generation computing.

Thomas Van Vaerenbergh received his masters degree in applied physics from Ghent University, Belgium, in 2010. He finished his PhD thesis on all-optical spiking neurons in the Photonics Research Group Gent university-imec in 2014. His PhD dissertation won the Alcatel-Lucent Bell Scientific Award 2015. Currently, he is a photonics research scientist in Hewlett Packard Labs at Hewlett Packard Enterprise, where he works on optical computing based on silicon photonics. His main research interests are layout automation for and simulation of large scale photonic integrated circuits (PIC), nonlinear dynamics in optical components, neuromorphic computing and modeling and design of passive PIC building blocks such as microrings and grating couplers.

Alexander Gazman received the B.S. in Electrical Engineering from Boston University in 2013 and the M.S. in Electrical Engineering from Columbia University in 2015. He is currently a PhD candidate in the Lightwave Research Laboratory at Columbia University. His research focuses on developing Silicon Photonic subsystems and integration of optical interconnects in high-performance compute systems.

Qixiang Cheng received his B.S. from Huazhong University of Sci. & Tech., China in 2010 and Ph.D. from the University of Cambridge, UK studying III/V integrated optical switches in 2014. He then stayed as a research assistant until March 2015, he joined Shannon Lab., Huawei, China researching future optical computing systems. He is now a postdoctoral research scientist in the Lightwave Research Lab at Columbia University, US with research interests in silicon photonic integrated circuits for high-capacity optical interconnects in supercomputers and data-centers.

Robert Polster received his Ph.D. from the Université Paris Sud in 2015 for his research on silicon photonic links that was carried out at the CEA-LETI in Grenoble, France. He received his M.S. degree in physics from the Humboldt University, Berlin, Germany in 2012. His master's thesis was carried out at the Institute for Quantum Optics and Quantum Information Theory (IQOQI) in Vienna from 2011-2012. He carried out further studies at the Paul-Scherrer-Institut / ETH Zurich and in the high field laser laboratory of the Max-Born-Institute in Berlin from 2006-2009. He is currently leading AIM Photonics functional testing program. His team's responsibilities are the standardization of supported test geometries, the design of test structures and the general bootstrapping efforts for AIM Photonics testing facility.

Keren Bergman (S'87-M'93-SM'07-F'09) received the B.S. degree from Bucknell University, Lewisburg, PA, in 1988, and the M.S. and Ph.D. degrees from Massachusetts Institute of Technology, Cambridge, in 1991 and 1994, respectively, all in electrical engineering. She is currently the Charles Batchelor Professor of Electrical Engineering at Columbia University, New York, where she is also the Scientific Director of the Columbia Nano Initiative (CNI). Her current research interests include optical interconnection networks for high performance embedded computing, optical data center networks, and silicon photonic systems-on-chip.